Article:

Laura Santamaria, Gartzen Lopez, Aitor Arregi, Maite Artetxe, Maider Amutio, Javier Bilbao, Martin Olazar, ***Catalytic steam reforming of biomass fast pyrolysis volatiles over Ni–Co bimetallic catalysts***. J**ournal of Industrial and Engineering Chemistry** 91 : 167-181 (2020)

Received 27 April 2020, Revised 27 July 2020, Accepted 28 July 2020, Available online 11 August 2020.

https://doi.org/10.1016/j.jiec.2020.07.050

Catalytic steam reforming of biomass fast pyrolysis volatiles over Ni-Co bimetallic catalysts

Laura Santamaria[a], Gartzen Lopez[a,b]*, Aitor Arregi[a], Maite Artetxe[a], Maider Amutio[a], Javier Bilbao[a] and Martin Olazar[a]

[a]Department of Chemical Engineering, University of the Basque Country UPV/EHU, P.O. Box 644 - E48080 Bilbao (Spain). gartzen.lopez@ehu.eus

[b]IKERBASQUE, Basque Foundation for Science, Bilbao, Spain

Abstract

The influence of the metal selected as catalytic active phase in the two-step biomass pyrolysis-catalytic reforming strategy has been analyzed. The pyrolysis step was carried out in a conical spouted bed reactor at 500 ºC, whereas steam reforming was performed in a fluidized bed reactor at 600 ºC. Ni/Al_2O_3, Co/Al_2O_3 and two bimetallic $Ni-Co/Al_2O_3$ catalysts with different metal loadings were synthesized by wet impregnation method, and fresh and deactivated catalysts were characterized by N_2 adsorption/desorption, X-ray Fluorescence (XRF), Temperature Programmed Reduction (TPR), X-Ray powder Diffraction (XRD), Temperature Programmed Oxidation (TPO), Scanning Electron Microscopy (SEM) and Transmission Electron Microscopy (TEM). Although Ni/Al_2O_3 and both bimetallic catalysts had similar initial activity in terms of (oxygenate conversion, (higher than 98%), the poorer metal dispersion observed in both bimetallic catalysts led to a fast decrease in conversion due to the promotion of coke formation on large particles. This occurred even though Ni-Co alloy formation has a positive influence by hindering the oxidation of Co^0 species. The main cause for the deactivation of these catalysts is the formation of a coke with amorphous structure. The poor initial performance of Co/Al_2O_3 catalyst is related to changes in the Co^0 oxidation state induced by the presence of steam, which led to a fast deactivation of this catalyst.

Keywords: hydrogen; pyrolysis; reforming; biomass; bimetallic catalysts, cobalt

1. Introduction

The growing energy demand and the increasing awareness of the dependence on fossil fuels are promoting the use of alternative routes for the production of clean energy from sustainable fuels and raw materials. Currently, almost 80 % of the global primary energy demand is supplied by crude oil, natural gas and coal [1]. Thus, the development of technologies for H_2 production can help to reduce CO_2 emissions, and therefore alleviate the problems associated with global warming and climate change.

The renewable nature of the biomass raw material along with its abundance and CO_2 neutral contribution are promoting the investigation of this feedstock for the production of hydrogen or synthesis gas [2-4], automotive fuels [5,6] and fine chemicals [7,8]. Consequently, the development of technological routes for obtaining H_2 from biomass has deserved a remarkable attention in the literature [3,9-12].

Two major routes are worth mentioning for the conversion of biomass into H_2, namely, thermochemical and biological processes [13]. The technologies for H_2 production from thermochemical processes, such as steam gasification and reforming of the bio-oil obtained in the flash pyrolysis of biomass, are the most studied in the literature [14-17]. Thus, they are relatively easy to scale up to industrial units for the conversion of biomass and bio-oil into valuable fuels and chemicals [18], which in turn bear similarities with the already implemented systems in oil refineries. Furthermore, the in-line steam reforming of the volatiles from biomass fast pyrolysis has been proven to be a promising route for H_2 production, since it has several advantages, as are: i) operation under optimum conditions due to the integration of the two reactors in the same unit, ii) avoidance of tar formation, and iii) higher H_2 production [19-21].

However, the catalyst performance and its deactivation plays a key role in the development of these processes based on the reforming of biomass derived products.

Over the last decades, the mechanisms and causes of catalyst activity decay have been extensively analyzed in order to establish the bases for modeling deactivation processes, improving catalyst design and preventing or slowing the degradation of the catalyst [22-25]. The causes of catalyst deactivation can be ascribed to three main factors: i) mechanical, (attrition/entrainment), ii) thermal, (sintering), and iii) chemical, (poisoning, coking, phase changes) [26]. However, deactivation is not the consequence of only one of the mentioned mechanisms, but usually their combination is responsible for the catalyst degradation.

The design of a suitable reforming catalyst is of utmost importance for the performance in terms of activity, selectivity and stability under reaction conditions [27-29]. Consequently, the selection of suitable catalytic materials is one of the most important factors for catalyst synthesis. Accordingly, given that the active components are responsible for the main chemical reaction, the metals selected as active phase should promote reforming and WGS reactions in order to enhance H_2 production in the reforming step. Ni-based catalysts have been the most widely used in the literature for CH_4 and naphtha reforming [30-32], as well as for the reforming of the oxygenated compounds derived from biomass pyrolysis [33-36] due to their high activity in the reforming reactions and moderate cost. Besides, other base transition metals, such as Co or Fe and, especially, noble metals, such as Rh, Pt, Pd, Ir and Ru, have also been studied in the literature [37-40], and they have even been added as secondary metals to prepare bimetallic catalysts, with the aim of improving catalytic activity and coke resistance.

Although great effort has been made in the literature regarding catalyst design for the reforming of oxygenated compounds derived from biomass pyrolysis, most of these studies have been conducted using model compounds instead of raw bio-oil or the whole pyrolysis volatile stream [41-43]. Besides, the selection of cobalt as active phase

and the influence its incorporation into Ni based catalysts has on the biomass pyrolysis-reforming strategy has hardly been studied. Thus, Li et al. [44] studied different Co based catalysts supported on Al_2O_3, ZrO_2, SiO_2, MgO, TiO_2 and $BaAl_{12}O_{19}$ (BA) in the steam reforming of the tar from the pyrolysis of wood biomass. The highest catalytic activity was obtained when Co/BA was used, which was attributed to the high dispersion obtained on this strongly basic support.

The addition of various transition metals to form different alloys has been approached by other authors in order to improve the overall activity of the catalysts. Accordingly, the performance of Ni-Fe/Al_2O_3 catalysts in the steam reforming of the tar from the pyrolysis of cedar wood was analyzed by Wang et al. [45], obtaining higher activity than those corresponding to monometallic Ni and Fe catalysts. The alloy formed between Ni and Fe improved the reaction involving the tar and hindered coke formation, since oxygen atoms are supplied by Fe species. This research group also analyzed the performance of Fe-Co/Al_2O_3, reporting a higher activity and stability of this catalyst compared to Fe/Al_2O_3 and Co/Al_2O_3 ones [46]. Similarly, these authors evaluated different Ni–Co/Al_2O_3 catalysts and observed that the performance of bimetallic catalysts with the optimum composition was much better than monometallic Ni and Co catalysts in terms of catalytic activity, resistance to coke formation and catalyst life in the steam reforming of biomass tar [47].

In previous studies conducted by our research group, the influence different support materials (Al_2O_3, SiO_2, MgO, TiO_2 and ZrO_2) [48] and promoters (La_2O_3, CeO_2 and MgO) [49,50] have on Ni-based catalysts was analyzed in the biomass pyrolysis and in-line steam reforming. This study deals with the effect the active phase has on the performance of the catalysts in an original unit made up of a conical spouted bed reactor for the pyrolysis step and a fluidized bed reactor for the reforming of the volatiles

formed in the first step. Accordingly, Ni/Al_2O_3, Co/Al_2O_3 and two bimetallic Ni-Co/Al_2O_3 catalysts with different Ni/Co loadings have been studied. The initial activity of the prepared catalysts at zero time on stream was evaluated. Moreover, the evolution of their performance throughout reaction time was monitored and a detailed characterization of all these catalysts was carried out in order to analyze their deactivation based on the properties of the fresh and deactivated catalysts.

2. Experimental

2.1. Materials and catalyst synthesis

Pine wood (pinus insignis) is the biomass selected in this study, as it is one of the most representative forest residues in Europe. In order to guarantee continuous feeding into the reaction system, the biomass has been crushed and sieved to a particle size ranging from 1 to 2 mm.

Table 1 summarizes the results obtained in previous studies for the ultimate and proximate analyses [51,52] determined in a LECO CHNS-932 elemental analyzer and in a thermogravimetric analyzer (TA Instrument TGA Q5000IR), respectively. The chemical composition of the ashes has been quantified by X-ray Fluorescence (AXIOS, PANalytical).The higher heating value (HHV) was measured in a Parr 1356 isoperibolic bomb calorimeter. As observed in Table 1, the amount of N in the wood sawdust is almost negligible, and therefore the empirical formula of the biomass is as follows: $CH_{1.47}O_{0.67}$.

Table 1. **Pine wood sawdust characterization.**

Ultimate analysis (wt. %)	
Carbon	49.33
Hydrogen	6.06
Nitrogen	0.04
Oxygen	44.57
Proximate analysis (wt. %)	
Volatile matter	73.4
Fixed carbon	16.7
Ash	0.5
Moisture	9.4
HHV (MJ kg^{-1})	19.8
Chemical analysis of the ash (wt. %)	
SiO_2	8.84
Al_2O_3	2.38
Fe_2O_3t	2.30
MnO	2.46
MgO	10.44
CaO	32.34
Na_2O	1.93
K_2O	11.30
TiO_2	0.11
P_2O_5	2.55
SO_3	3.59
Trace elements (ppm)	
Ni	4249
Zn	1734
Cu	5146

The catalysts synthesized in this study were Ni/Al_2O_3, Co/Al_2O_3 and two bi-metallic Ni-Co/Al_2O_3 catalysts with different metal loadings. Prior to catalyst synthesis, the γ-Al_2O_3 support was adequately pre-treated in order to ensure suitable fluidization conditions in

the reforming step [51]. Accordingly, the support was ground and sieved to a particle size in the 0.4–0.8 mm range since this size was determined as the most suitable one for use in fluidized bed reforming reactors [51]. The support was fluidized for several hours in order to round the particles, thereby improving their mechanical strength and minimizing possible attrition problems during the reforming step. Afterwards, the γ-Al_2O_3 support was calcined under air atmosphere at 1000 ºC for 5 h to thermally stabilize the support and improve its mechanical strength.

The monometallic Ni and Co based catalysts supported on Al_2O_3 were prepared by wet impregnation using an aqueous solution of $Ni(NO_3)_2 \cdot 6H_2O$ (VWR Chemicals, 99 %) and $Co(NO_3)_2 \cdot 6H_2O$ (Panreac AppliChem, 98-102 %), respectively. Subsequently, the samples were dried overnight at 100 ºC followed by calcination at 700 ºC for 3 h under air atmosphere. The synthesis of the bimetallic catalysts was carried out by impregnation of the aqueous solutions containing both salt precursors, with the amounts of each one being those required to attain the desired final composition of the catalyst. Accordingly, the nominal metal content in all the catalysts has been fixed at 10 wt. % of the Al_2O_3 support, as this is the optimum value reported in the literature for Ni/Al_2O_3 catalysts [53]. The loadings of bimetallic catalysts were 7.5% Ni-2.5% Co and 5% Ni-5% Co, given as wt. % of the Al_2O_3 support. After impregnation, the samples were dried overnight at 100 ºC followed by calcination at 700 ºC for 3 h under air atmosphere.

2.2. Characterization of the fresh and deactivated catalyst

N_2 adsorption-desorption technique was carried out in a *Micromeritics ASAP 2010 apparatus* in order to determine the textural properties of the fresh and deactivated catalysts (surface area, pore volume and average pore diameter). Prior to analysis, the samples were degassed under vacuum at 150 °C for 8 h to remove any impurity in the

sample. Surface area was calculated based on the BET equation, whereas the pore size distribution was determined by BJH method.

The total metal loading (wt. %) of each catalyst was measured by means of X-ray fluorescence (XRF) spectrometry. The chemical analysis was carried out under vacuum atmosphere using a sequential wavelength dispersion X-ray fluorescence (WDXRF) spectrometer *(Axios 2005, PANalytical)* equipped with a Rh tube, and three detectors (gaseous flow, scintillation and Xe sealing).

The reduction temperature of the different metallic phases in the catalyst was analyzed by Temperature Programmed Reduction (TPR) in a *Micromeritics AutoChem 2920.* Prior to the reduction experiments, the catalysts were thermally treated under He stream at 200 °C in order to remove water or any impurity. Then, a 10 vol. % of H_2/Ar stream circulated through the sample, which was heated from room temperature to 900 ºC following a ramp of 5 ºC min^{-1}.

The analysis of the crystalline structure of the calcined, reduced and deactivated catalysts has been performed by X-ray powder diffraction (XRD) in a *Bruker D8 Advance diffractometer* with a CuKα1 radiation equipped with a Germanium primary monochromator and Sol-X dispersive energy detector. Data were continuously registered from 10° to 80° with steps of 0.04° in 2θ and measurement times per step every 12s. The metal crystallite size was calculated by using the Scherrer formula. Metal dispersion was calculated from metal crystallite size according to the following equation [54]:

$$D\ (\%) = \frac{M_M \cdot g}{\rho_M \cdot \sigma_M \cdot N_A \cdot d_M\ (nm)} \cdot 100 \qquad (1)$$

where M_M is the atomic weight of the metal (g mol^{-1}), g a factor depending on particle shape (g = 6 for spherical particles), ρ_M the specific mass of the metal, σ_M the atomic surface area (0.0677 nm^2 at^{-1} for Ni particles and 0.0685 nm^2 at^{-1} for Co particles, [55,56]), N_A Avodagro's number and d_M the crystallite size calculated by XRD analysis.

Accordingly, the dispersion for monometallic Ni/Al_2O_3 and Co/Al_2O_3 catalysts can be calculated as A_M/d_M (nm)·100, wherein A_{Ni} = 0.971 and A_{Co}= 0.963. In the bimetallic catalysts, Ni and Co contents (wt. %) are taken into account as follows [57]:

$$D\ (\%) = \frac{\left[\frac{A_{Ni}\cdot Ni}{(Ni+Co)} + \frac{A_{Co}\cdot Co}{(Ni+Co)}\right]}{d_M(nm)}\cdot 100 \qquad (2)$$

Furthermore, the amount of coke deposited on the deactivated catalysts was measured by Temperature Programmed Oxidation (TPO) in a *TA Instruments TGA Q5000* thermogravimetric (TG) apparatus, coupled in-line with a *Balzers Instruments Thermostar* mass spectrometer (MS). This device allows recording the signals at 14, 18, 28 and 44 atomic numbers, corresponding to N_2, H_2O, CO and CO_2, respectively. The coke content has been determined based on the CO_2 signal, since the H_2O formed during combustion and that corresponding to the moisture cannot be distinguished and, furthermore, CO is immediately oxidized to CO_2 activated by the metallic function of the catalyst. The procedure entails the stabilization of the signal with a N_2 stream (50 mL min^{-1}) at 100 ºC and subsequent oxidation with air (50 mL min^{-1}), following a ramp of 5 ºC min^{-1} to 800 ºC and keeping this temperature for 30 min to guarantee total coke combustion.

Moreover, as the duration of the experimental runs was not the same, the average coke deposition rate per biomass mass unit fed has been defined in order to compare the amounts of coke deposited on the different catalysts, as follows:

$$\bar{r}_{coke} = \frac{W_{coke}/t}{W_{catalyst}\, m_{biomass}} \quad (3)$$

with $W_{catalyst}$ and W_{coke} being the catalyst and coke masses, respectively, $m_{biomass}$ the biomass mass flow rate in the feed and t the reaction time in each run.

In addition, Scanning Electron Microscopy (SEM) and Transmission Electron Microscopy (TEM) were carried out in order to determine the nature and location of the coke deposited on the catalyst. Hence, SEM images were obtained in a *JEOL JSM-6400* apparatus, with a W filament, and the nanometer level images of the catalysts were obtained using a *Transmission Electron Microscope* (TEM) (*Philips CM200)* with a supertwin lens fitted with an EDX microanalysis system (Energy-Dispersive X-ray spectroscopy).

2.3. Reaction equipment and experimental conditions

The scheme of the bench scale plant used in the experimental runs is shown in Figure 1. The reaction system is provided with two reactors in-line: a conical spouted bed reactor (CSBR) and a fluidized bed reactor (FBR). The biomass pyrolysis was carried out in the first reactor, namely the CSBR, whose good performance in the pyrolysis of biomass [58-60], tyres [61,62] and plastics [63,64] was reported in previous studies. The volatiles leaving the first pyrolysis step (gases and bio-oil oxygenated compounds), circulated towards the second reactor (FBR) to be catalytically reformed. In order to avoid the condensation of the volatile stream and the reforming products, both reactors and its respective radiant ovens are located inside a convection oven kept at 270 °C. Moreover, the CSBR is provided with a lateral outlet pipe placed above the bed surface for the removal of char particles from the bed (Figure 1). This two-step configuration also demonstrated to operate well in previous pyrolysis-reforming studies, wherein a detailed description of the reactors can be found [48,65,66].

The reaction equipment is provided with different devices, which allow continuous feeding of biomass, water and gases (N_2, air, H_2). The solid feeding system is made up of a cylindrical vessel equipped with a vertical shaft connected to a piston placed below the material bed. As the piston raises, the biomass falls onto the bed in the reactor through a tube cooled with tap water. The water required in the reforming step was introduced in the pyrolysis reactor by means of a high precision Gilson 307 pump and, prior to entering the forced convection oven, the water was vaporized using a heating cartridge located inside the hot box. Previous studies demonstrated the inert nature of steam when used as fluidizing agent instead of N_2, which allows avoiding the dilution of the gaseous stream in the reforming reactor and easing the condensation of the volatile products (non-reacted oxygenates and water) [51]. Moreover, different gases (N_2, air and H_2) can also be fed into the lower part of the pyrolysis reactor. Thus, N_2 was used as fluidizing agent during the heating process and H_2 was employed to reduce the Ni catalyst prior to the reforming reaction. It is to note that once the reaction temperature was reached, the fluidizing agent was changed from N_2 to steam, and biomass was not fed until an adequate fluidization was attained in both reactors. The bench scale plant was also provided with a particle separation system made up of a cyclone, a filter and a liquid-gas separation system provided with a condenser and a coalescence filter.

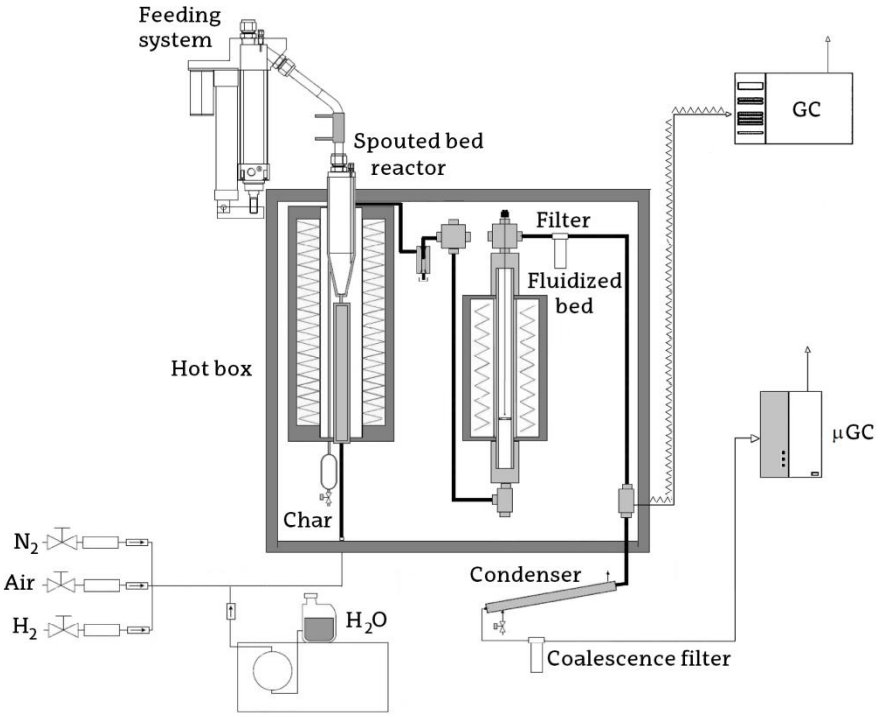

Figure 1. Diagrammatic representation of the bench scale plant for continuous pyrolysis-reforming of biomass.

The analysis of the product stream is carried out in-line by means of a *Varian 3900 GC* for volatile products, and a *Varian 4900 microGC* for permanent gases. The gas chromatograph (*Varian 3900*) is outfitted with a HP-Pona column and a flame ionization detector (FID), and the sample is taken at the outlet of the FBR, prior to condensing the products. The gas micro-chromatograph (*Varian 4900*) is equipped with four different analytical modules (Molecular sieve 5, Porapack, CPSil and Plot Alumina) and thermal conductivity detectors (TCD), and the non-condensable sample is taken downstream the condensation system, which allows determining the concentration of the products not monitored by GC analysis.

The optimum operating conditions in the biomass pyrolysis-reforming process were established based on previous experiments performed by the research group [51,67]. As aforementioned, steam is used as fluidizing agent in both steps, and therefore, in order

to ensure an adequate fluidization regime, the steam flow rate and the particle sizes of the inert and the catalyst that make up the beds in the CSBR and FBR were carefully selected. Accordingly, 30 g of silica sand with a particle size in the 0.3-0.35 mm range were introduced in the CSBR, whereas 25 g of a mixture of reforming catalyst and sand (50 wt. %) were place in the FBR bed, which accounts for a space time of 20 g_{cat} min $g_{volatiles}^{-1}$. The particle sizes used are in the 0.4-0.8 mm and 0.3-0.35 mm ranges for the catalyst and the sand, respectively. Prior to the experimental runs, the catalysts were subjected to an in situ reduction process at 710 ºC for 4 h under H_2 stream (10 vol. %) diluted with N_2.

The water flow rate used in all the experiments was 3 mL min^{-1}, which corresponds to a steam flow of 3.73 NL min^{-1}. Biomass was continuously introduced into the pyrolysis-reforming unit, with a feed rate of 0.75 g min^{-1}, which corresponds to a steam/biomass (S/B) ratio of 4, and a steam/carbon (S/C) molar ratio of 7.7 in the reforming step. It is to note that the amount of carbon contained in the char formed in the pyrolysis step was not considered in the calculation of this ratio.

Besides, biomass pyrolysis temperature was selected based on the experience of the research group. Thus, the pyrolysis step was conducted at 500 ºC, as this temperature is the optimum one to maximize bio-oil yield [58]. The products obtained in the biomass pyrolysis were identified and quantified in previous studies, and the concerning details can be found elsewhere [51,58]. As aforementioned, the inert nature of steam as fluidizing agent in the first step was verified operating under mild pyrolysis conditions [51], and the products obtained in the pyrolysis at 500 ºC can be grouped as follows: i) bio-oil (75.3 wt. %), which is made up of phenols (16.5 wt.%), ketones (6.4 wt.%), saccharides (4.5 wt.%), furans (3.3 wt.%), acids (2.7 wt.%), alcohols (2.0 wt.%), aldehydes (1.9 wt.%) and water (25 wt.%) (the reforming agent in the second step); ii)

gases (7.3 wt. %), made up of mainly CO (3.4 wt.%) and CO_2 (3.3 wt.%); and, iii) char (17.3 wt. %), which was continuously removed from the pyrolysis reactor through a lateral outlet pipe, and therefore the secondary reactions of pyrolysis volatiles on the char surface were minimized leading to a maximum oxygenate yield and enhancing the char quality for future applications [68]. Thus, the volatile stream to be reformed in the second step was made up of bio-oil oxygenated compounds and gaseous products.

Similarly, the temperature selected for the reforming step was fixed at 600 ºC, since higher temperatures (700 ºC) hardly improve the experimental results [51], but increase energy requirements and may lead to metal sintering. Thus, the influence of temperature on metal sintering is correlated with Tamman temperature, which corresponds to 590 ºC (863 K) and 604 ºC (877 K) for Ni and Co based catalysts, respectively [24].

2.4. Reaction indices

The performance of the synthesized catalysts has been evaluated based on the conversion and individual product yields as the foremost reaction indices. It is to note that these reaction indices are defined based on the pyrolysis volatiles fed into the reforming step (gases and bio-oil oxygenated compounds), rather than on the biomass fed into the pyrolysis step, i.e., the conversion in the reforming step does not consider the carbon contained in the char produced in the pyrolysis step, since this product was removed from the process prior to the reforming step.

Consequently, the oxygenate conversion in the reforming reactor is defined as the ratio between the C moles in the gaseous product (C_{gas}) stream and the C moles in the volatile stream at the fluidized bed reactor inlet ($C_{volatiles}$):

$$X = \frac{C_{gas}}{C_{volatiles}} 100 \quad (4)$$

Likewise, the yield of each carbon containing gaseous product is calculated as the ratio between the molar flow rate of compound i (F_i) and the molar flow rate of the volatile stream at the fluidized bed reactor inlet ($F_{volatiles}$):

$$Y_i = \frac{F_i}{F_{volatiles}} 100 \quad (5)$$

The hydrogen yield was defined based on the maximum allowable by stoichiometry:

$$Y_{H_2} = \frac{F_{H_2}}{F^0_{H_2}} 100 \quad (6)$$

where F_{H2} is the H_2 molar flow rate and F^0_{H2} the maximum allowable by the following stoichiometry:

$$C_nH_mO_k + (2n-k)H_2O \rightarrow nCO_2 + (2n+m/2-k)H_2 \quad (7)$$

The H_2 production is defined by mass unit of the biomass in the feed:

$$\text{Prod. } H_2 = \frac{m_{H_2}}{m^0_{Biomass}} \, 100 \quad (8)$$

where m_{H2} and m^0 are the mass flow rates of H_2 produced and biomass fed into the process, respectively.

Finally, the turnover frequency (TOF) expressed in moles in the gaseous product (C_{gas}) stream per mole of surface metal active site and min is determined as follows:

$$TOF = \frac{\frac{C_{gas}}{C_{volatiles}} \cdot F_{volatiles} \cdot AW_{Me}}{W \cdot D \cdot Me_{content}} \quad (9)$$

where $F_{volatiles}$ is the molar flow rate of the volatile stream ($mol_{volatiles}$ min^{-1}), AW_{Me} is the atomic weight of the metal (g_{Me} mol_{Me}^{-1}), W is the mass of catalyst (g_{cat}), D is the dispersion calculated from Eqs (1) and (2), and $Me_{content}$ is the metal content of each catalyst determined by XRF analysis.

3. Results

3.1. Effect of the metal active phase on the catalysts properties

3.1.1. Physical properties

The influence the metal active phase has on the catalyst's features has been analyzed by means of a detail characterization. Accordingly, the textural properties of the Al_2O_3 support and the prepared catalysts were determined by N_2 adsorption-desorption technique and are displayed in Table 2. As observed, the support used is a mesoporous material, with an average pore size of 173 Å. Once the active phase (Ni, Co, or a Ni/Co mixture at different ratios) has been incorporated into the Al_2O_3 support, a decrease in BET surface area is observed in all the prepared catalysts as a result of the blockage caused by metal species deposition on the pores of the support [69,70]. Pore volume

scarcely increased in the Ni/Al_2O_3 catalyst compared to the starting support (varied from 0.38 for the support to 0.39 $cm^3\ g^{-1}$ for the catalyst), whereas a marked decrease is observed when Co is used, either in the monometallic or bimetallic catalysts. This fact is attributed to the formation of Co_3O_4 molecules, detected by XRD analyses (details will be given below), instead of NiO, which leads to the blockage of the Al_2O_3 porous structure. It is to note that a similar pore volume was obtained for the catalysts in which cobalt was incorporated as active phase (0.33 $cm^3\ g^{-1}$). Papageridis et al. [71] observed a decrease in both surface area and pore volume when cobalt was impregnated on the Al_2O_3 support.

Table 2. Physical properties of the support and prepared catalysts.

Catalyst	$\mathbf{S_{BET}}$ **($m^2\ g^{-1}$)**	$\mathbf{V_{pore}}$ **($cm^3\ g^{-1}$)**	$\mathbf{d_{pore}}$ **(Å)**
Al_2O_3	87	0.38	173
Ni/Al_2O_3	76	0.39	182
$7.5Ni\text{-}2.5Co/Al_2O_3$	79	0.33	164
$5Ni\text{-}5Co/Al_2O_3$	78	0.33	170
Co/Al_2O_3	75	0.33	177

The average pore sizes in Ni/Al_2O_3 and Co/Al_2O_3 catalysts increased from 173 Å (corresponding to the support) to 182 and 177 Å, respectively, which suggests that the metallic phase was mainly deposited on the finest pores. Conversely, the pore size of the bimetallic catalysts decreased due to the blockage of the biggest pores, presumably by the interaction between NiO and Co_3O_4 formed during the calcination step in the catalyst synthesis.

3.1.2. Reducibility of metallic species

The temperature programmed reduction (TPR) profiles of the prepared catalysts are shown in Figure 2. It is well established that catalyst reducibility is strongly dependent on the nature of the metal function, which is also evident in these profiles.

The reduction profile of Ni/Al_2O_3 catalyst shows two main peaks located at 620 ºC and 780 ºC, with the former corresponding to the reduction of highly dispersed and strongly interacting NiO, and the latter to Ni integrated in the $NiAl_2O_4$ spinel phase [72,73]. Moreover, a small peak at lower temperature (430 ºC) is also evident, which is associated with the reduction of NiO with weak interaction with the Al_2O_3 support [74].

Concerning the Co/Al_2O_3 catalyst, two main peaks can be distinguished in the TPR profiles, which are located at around 450 and 700 ºC, and are ascribed to the reduction of different cobalt species. According to the literature, the reduction of cobalt based catalysts follows a two-step process, as is: $Co_3O_4 \rightarrow CoO \rightarrow Co^0$ [75,76]. Thus, several authors grouped the different reducible species observed in the TPR analysis according to their reduction temperature as follows: i) 250–350 ºC: reduction of Co_3O_4 to CoO, ii) 375–600 ºC: reduction of CoO to Co^0; and iii) > 700 ºC: reduction of $CoAl_2O_4$ crystallites, which is due to the strong interaction between Co_3O_4 and the support, and occurs by the introduction of Co (II) in the tetrahedral vacancies of the defect spinel structure of alumina [71,77]. However, the location of the reduction peaks, and therefore the metal-support interaction greatly depends on the calcination temperature during the synthesis step. Thus, higher calcination temperatures hinder the reducibility of the metallic species by shifting reduction peaks to higher temperatures in the TPR analysis [78,79].

Furthermore, other authors compared the reduction peaks of Co/Al_2O_3 catalyst with those of reference materials, and they concluded that the first peak located at low temperature (sharp peak) is related to the fast reduction of Co_3O_4 to CoO, whereas the

broad second peak, which may range up to 730 ºC, should be ascribed to the slow reduction of CoO to Co^0 [75,80-82].

Given the uncertainty in the identification of the reducible species in the literature, these TPR profiles have been complemented with the information from the XRD technique (Figure 3), which allows classifying the reduction peaks following the first reduction mechanism explained above. Thus, it can be observed that the main peak obtained at 450 ºC is provided with a shoulder at around 510 ºC, which corresponds to the reduction of cobalt oxides to metallic Co^0 according to the two-reduction step, with both steps taking place almost simultaneously ($Co_3O_4 \rightarrow CoO \rightarrow Co^0$) [83]. The second peak also contains a shoulder at high temperature (at around 800 ºC), which is ascribed to the transformation of residual cobalt oxides and $CoAl_2O_4$ species with different degrees of interaction with supported alumina species [84].

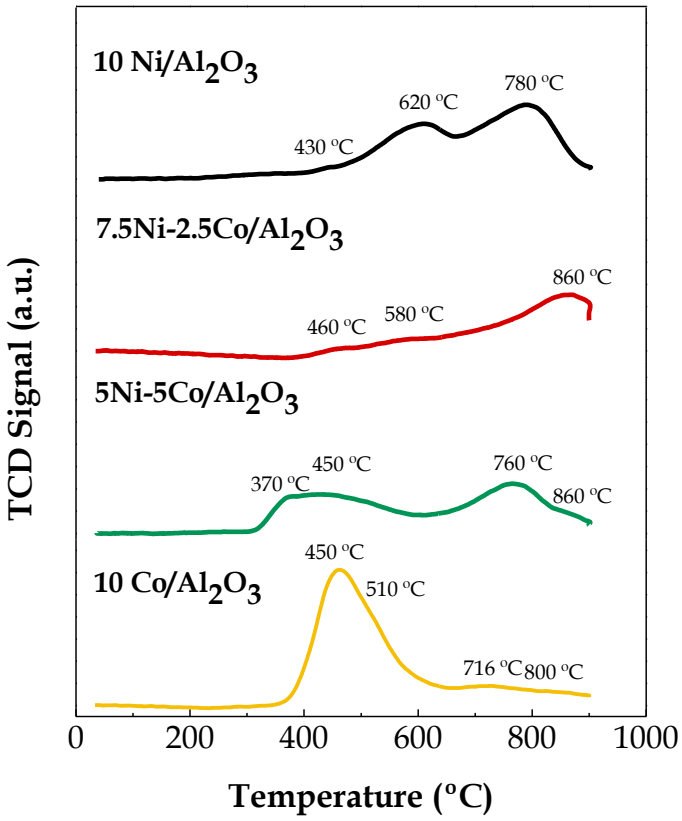

Figure 2. TPR profiles of the prepared catalysts.

The reduction profiles of the bimetallic catalysts are significantly different from each other, revealing the influence the Ni/Co loading ratio has on the reducibility of the catalyst. In the case of 5Ni-5Co/Al_2O_3 catalyst, four different peaks are observed, which are located at 370 ºC, 450 ºC, 760 ºC and 860 ºC, with the first two ones being attributed to the reduction of NiO and Co_3O_4 species, respectively, and those at higher temperatures corresponding to the reduction of spinel phases ($NiAl_2O_4$ and $CoAl_2O_4$) [70].

Moreover, the comparison between the TPR profiles of the monometallic Ni/Al_2O_3 and Co/Al_2O_3 catalysts and the bimetallic 5Ni-5Co/Al_2O_3 catalyst reveals that the reduction peaks of the latter shift to lower temperatures, which is evidence of the capability of bimetallic catalysts to promote the reducibility of the metal oxides by modifying the interaction between the active phase and the support [70]. This trend was also observed by Chen et al. [85], who reported an improvement in Co reducibility when Ni was added to the catalyst.

Similarly, the 7.5Ni-2.5Co/Al_2O_3 catalyst showed three main peaks at 460, 580 and 860 ºC, which are ascribed to the reduction of NiO, Co_3O_4 and Ni and/or Co species, which are strongly interacting with the support forming spinel phases ($NiAl_2O_4$ and $CoAl_2O_4$).

3.1.3. Chemical composition and metallic properties

The chemical composition (Ni and Co content) and the metallic properties (metal crystallite size and dispersion) of all synthesized catalysts are shown in Table 3. The chemical composition was determined by XRF spectrometry, and the results reveal that the metal content in all the catalysts was close to the nominal loading, with the total amount of active phase being 10 wt. %, which is evidence that the wet impregnation method is suitable for catalysts synthesis.

The metal dispersion of each catalyst prepared was estimated based on the metal crystallite size obtained by XRD analysis (by applying Debye-Scherrer equation) and the previously described methodology (Section 2.2) following Eqs. (1) and (2).

It is to note that although all the catalysts had similar BET surface area, i.e., between 75 and 79 m^2 g^{-1} (Table 2), they had significant differences in metal dispersion. This fact reveals that not only the surface area of the support, but also the features of the metal oxide selected as active phase influence the final metal dispersion on the catalyst.

Thus, monometallic Ni/Al_2O_3 and Co/Al_2O_3 catalysts had the highest metal dispersion, (9.7 and 7.4 %, respectively), whereas the incorporation of both Ni and Co active phases led to a significant decrease in metal dispersion in both bimetallic catalysts. These lower dispersion values obtained in the bimetallic catalysts may be ascribed to the synthesis method. Thus, Zhao and Lu [70] reported that the preparation method of bimetallic Ni-Co based catalysts greatly influences the surface dispersion of the metallic species over the support, and consequently, the catalytic performance in the steam reforming reaction.

Table 3 Metallic properties and chemical composition of the fresh catalysts.

Catalyst	Ni content (wt. %)	Co content (wt. %)	d_M[a] (nm)	Metal Dispersion[b] (%)
$10Ni/Al_2O_3$	9.79	-	10	9.7
$7.5Ni\text{-}2.5Co/Al_2O_3$	7.05	2.90	24	4.0
$5Ni\text{-}5Co/Al_2O_3$	4.83	5.31	24	4.0
$10Co/Al_2O_3$	-	11.20	13	7.4

[a] Calculated from the full width at half height of the diffraction peak of Ni^0 (2 0 0) and Co^0 (2 0 0) at $2\theta = 52°$ in the XRD, using the Scherrer equation.

[b] Dispersion calculated by XRD, based on the metal crystallite size, following Eqs. (1) and (2) [44,57].

Figure 3 shows the XRD patterns of the calcined fresh catalysts. As observed, the reflection peaks characteristic of the Al_2O_3 support are evident in all the catalysts prepared. In these profiles, the Ni/Al_2O_3 catalyst shows characteristic diffraction peaks of NiO at 2θ = 37°, 43° and 63°, corresponding to (1 1 1), (2 0 0) and (2 2 0) facets, respectively [86-88], whereas no reflections ascribed to $NiAl_2O_4$ are observed at 2θ = 19°, 45° and 60°, since these diffraction lines may overlap those of Al_2O_3 phase [79,89,90].

Regarding bimetallic catalysts, the calcined samples show diffraction lines related to Co_3O_4 phase at 2θ = 19º, 31º, 37º, 45º, 55º, 59º, and 65º, which are attributed to the planes (1 1 1), (2 2 0), (3 1 1), (4 0 0), (4 2 2), (5 1 1) and (4 4 0), respectively [86]. Moreover, main reflections ascribed to NiO phase are also evident at 2θ = 43° and 63º. It is to note that $NiCo_2O_4$ and Co_3O_4 have similar patterns and their differentiation is difficult, and this species ($NiCo_2O_4$) may therefore has been formed during the synthesis step instead of separate Co_3O_4 and NiO species.

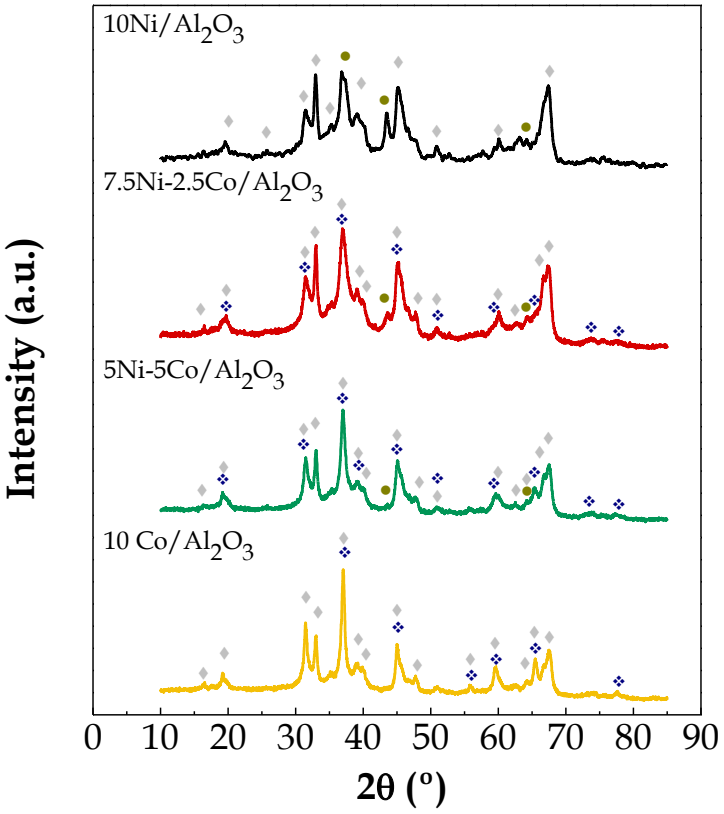

Figure 3. XRD patterns of the calcined catalysts. Crystalline phases: (♦) Al_2O_3, (●) NiO, and (❖) Co_3O_4.

In the case of Co/Al_2O_3 calcined catalyst, characteristic diffraction lines attributed to the Co_3O_4 phase are observed. The XRD patterns do not reveal diffraction peaks ascribed to $CoAl_2O_4$ spinel phase. Nevertheless, based on the TPR profiles, these diffraction lines and those of Co_3O_4 phase may overlap [91]. Besides, no diffraction peaks related to CoO are observed in the profiles of the calcined catalysts.

Figure 4 shows the XRD profiles of the catalysts reduced at 710 °C for 4 h. Two different profiles of Co/Al_2O_3 catalysts are shown in this Figure, with the second one corresponding to a reduced catalyst that has been subsequently subjected to a steam flow (details will be provided below). Thus, the characteristic diffraction peaks of Ni^0, Co^0 and Ni^0/Co^0 phases are observed in Ni/Al_2O_3, Co/Al_2O_3 and $Ni\text{-}Co/Al_2O_3$ catalysts,

respectively, at 2θ = 44°, 52° and 76°, which are ascribed to the planes (1 1 1), (2 0 0) and (2 2 0) [86,88]. Overlapping of the diffraction peaks for Co^0 and Ni^0 phases hinders their separate identification in the bimetallic catalysts.

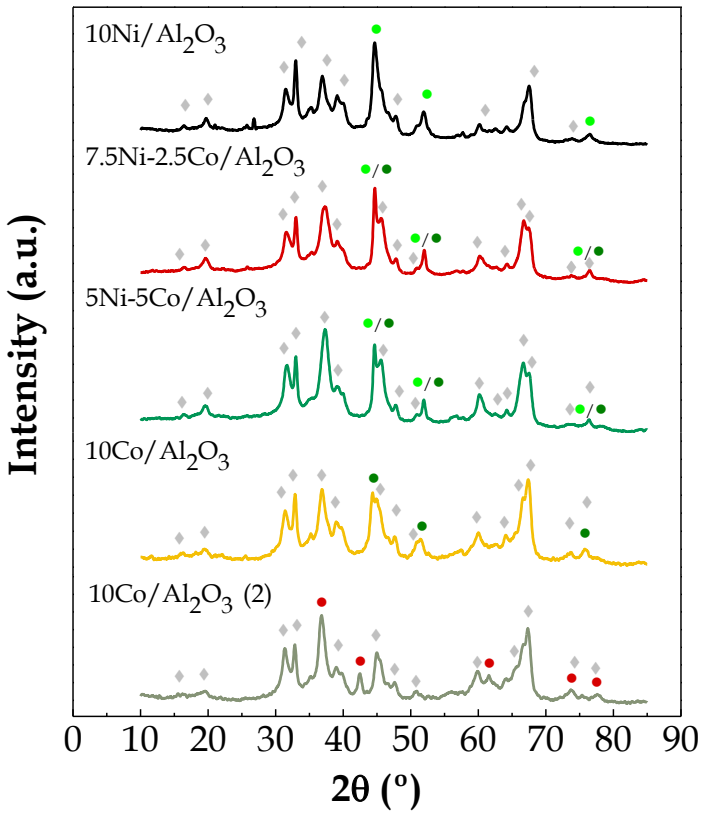

Figure 4. XRD patterns of the reduced catalysts. Crystalline phases: (♦) Al_2O_3, (●) Ni^0, (●) Co^0, and (●) CoO.

It is to note that no diffraction peaks corresponding to the oxidized species, such as NiO, Co_3O_4 and CoO, are observed in the XRD patterns, which means catalysts are fully reduced to the metallic species Ni^0 and Co^0.

3.2. Catalysts performance

With the aim of evaluating the influence the active phase has on the catalytic performance and stability of the different prepared catalysts, the evolution of oxygenate

conversion (Figure 5) and product yields (Figure 6) with time on stream was studied. Accordingly, the following reactions have been considered:

Oxygenate steam reforming:

$$C_nH_mO_k + (n-k)H_2O \rightarrow nCO + (n + m/2 - k)H_2 \quad (10)$$

Water Gas Shift (WGS):

$$CO + H_2O \leftrightarrow CO_2 + H_2 \quad (11)$$

Oxygenate cracking (secondary reaction):

$$C_nH_mO_k \rightarrow \text{oxygenates} + \text{hydrocarbons} + CH_4 + CO + CO_2 + C \quad (12)$$

Methane (and hydrocarbons) steam reforming:

$$CH_4 + H_2O \leftrightarrow CO + 3H_2 \quad (13)$$

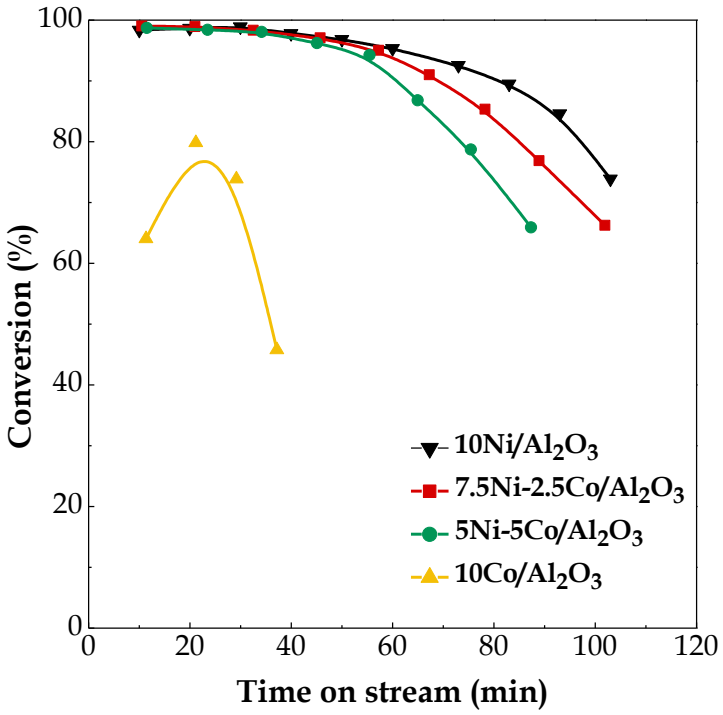

Figure 5. Effect of the active phase used for preparing Al_2O_3-supported catalysts on the evolution of oxygenate conversion with time on stream.

As observed in Figure 5, similar oxygenate conversion values were obtained at zero time on stream for Ni/Al_2O_3 catalysts (98.4 %) and both bimetallic $Ni\text{-}Co/Al_2O_3$ catalysts with different loading ratios (99.0 and 98.7 % for $7.5Ni\text{-}2.5Co/Al_2O_3$ and $5Ni\text{-}5Co/Al_2O_3$, respectively), which is evidence of the efficiency of these catalysts to reform the volatiles from the biomass pyrolysis. Nevertheless, a significant lower conversion was attained at the beginning of the experimental run when the Co/Al_2O_3 catalyst was tested (64.1 %), which is presumably a consequence of the oxidation state of the metallic phase, since the oxidizing nature of steam favours the conversion of Co^0 to cobalt oxide. As aforementioned, prior to feeding the biomass, the fluidizing agent was changed from N_2 to steam, which was maintained the time required to ensure adequate fluidization regime. Thus, changes in the oxidation state of the active catalytic phase may have been induced by the presence of steam. This hypothesis was also supported by Bayram et al. [92], who analyzed the state of cobalt species during the steam reforming of ethanol on a Co/CeO_2 catalyst, wherein they observed that metallic Co was partially oxidized to CoO during the steam reforming of ethanol on the reduction-pretreated catalyst. Similarly, Giehr et al. [93] carried out a thermodynamic study of the oxidation state of the active metals in $Co/\gamma\text{-}Al_2O_3$ and $Ni/\gamma\text{-}Al_2O_3$ catalysts under dry and steam reforming conditions, and they concluded that Ni oxidation by water under reforming conditions cannot occur spontaneously, but cobalt is more easily oxidized. With the aim of corroborating the oxidizing nature of steam and its effect on cobalt catalyst oxidation state, a steam flow was passed through the catalyst bed under reaction conditions, i.e., 600 ºC for 5 min, which was approximately the time required to attain a stable fluidization regime in both reactors prior to feeding the biomass. This sample was also analyzed by XRD technique, and the results are presented in Figure 4, in which the catalyst has been named as $10Co/Al_2O_3$ (2). In this profile, new diffraction

lines came out at 2θ = 37º, 42º, 61º, 74º and 77º, corresponding to the planes of (1 1 1), (2 0 0), (2 2 0), (3 1 1) and (2 2 2) of the fcc crystal structure of CoO [94]. Besides, the reflection peaks associated with Co^0 (which were observed in the sample reduced at 710 ºC) do not appear in this pattern, which is evidence of the oxidizing effect of steam on the Co/Al_2O_3 catalyst. Moreover, the absence of oxidized species (CoO and/or Co_3O_4) in the reduced sample shown in Figure 4 revealed the unfeasibility that this catalyst was oxidized by air before conducting the XRD analysis.

Moreover, significant differences are observed in the evolution of conversion with time on stream in the prepared catalysts. The Ni/Al_2O_3 catalyst had a better performance than both bimetallic Ni-Co based catalysts, with a stable activity for the first 30 min on stream and conversion decreasing to 73.9% subsequent to 103 min on stream. Similarly, $7.5Ni\text{-}2.5Co/Al_2O_3$ and $5Ni\text{-}5Co/Al_2O_3$ catalysts also revealed this stable activity period on the first 30 minutes (due to the high space time used in the runs), with a faster deactivation rate as the Ni/Co loading ratio was decreased (conversion values decreased from 99.0 to 66.2% after 102 min on stream and from 98.7 to 65.9 % after 87 min on stream for $7.5Ni\text{-}2.5Co/Al_2O_3$ and $5Ni\text{-}5Co/Al_2O_3$ catalysts, respectively). This fast decrease in oxygenate conversion is presumably a consequence of the significantly lower metal dispersion of both bimetallic catalysts compared to the monometallic catalysts (see Table 3). Thus, it is well established that large metal particles, i.e., catalysts with low metal dispersion, are known to promote coke formation, leading to the deactivation of the catalyst. In these runs, full conversion was observed for the first 30 min because there was catalyst excess. Besides, operation by continuously feeding the biomass needed certain time to attain steady state conditions (which is of the same order as catalyst deactivation), thereby requiring slightly higher space times to obtain reproducible results and analyze catalysts' activity. Thus, loss of activity was observed

after several minutes on stream. Besides, in order to analyze catalyst activity, the turnover frequency (TOF) has been determined for Ni/Al_2O_3 and both bimetallic catalysts according to Eq. (9). This reaction index has been calculated at 45 min on stream, as conversion values are below 100% at this time and coke deposition is expected to have little influence on the catalyst deactivation. The TOF corresponding to Co/Al_2O_3 catalysts was not determined because there were no Co^0 active sites during the reforming reaction. Thus, the TOF values decreased according to the following order: $7.5Ni2.5Co/Al_2O_3$ (24.6 min^{-1}) > $5Ni5Co/Al_2O_3$ (24.4 min^{-1}) > $10Ni/Al_2O_3$ (10.4 min^{-1}). According to these results, bimetallic catalysts have higher activity than the Ni/Al_2O_3 catalyst, and their faster deactivation will therefore be analysed in Sections 3.3 and 3.4.

In the case of Co/Al_2O_3 catalyst, oxygenate conversion peaks at 21 min on stream (79.8 %), which is a consequence of the reducing atmosphere in the reforming step leading to a reduction of cobalt species that were partially oxidized prior to feeding the biomass. Thus, this reduction provided the catalyst with more metallic active sites, which enhanced the capability for reforming the bio-oil oxygenate compounds derived from biomass pyrolysis. Subsequently, conversion sharply decreased to 45.8 % after 37 min on stream due to the strong reaction conditions, i.e., the Co/Al_2O_3 catalyst was exposed to high partial pressures of non-converted oxygenate compounds.

Figure 6 shows the evolution of the individual product yields with time on stream in the reforming step for all the catalysts prepared, i.e., H_2 yield calculated based on the maximum allowable by stoichiometry, Eq. (6), and the gaseous compound yields, Eq. (5). For a better visualization of the results, each one of these graphs has been divided into two parts, with the yields of hydrocarbons and methane being displayed in the lower part of each pair due to their low yield.

As observed, similar trends are observed for Ni/Al_2O_3 (Figure 6a) and $Ni\text{-}Co/Al_2O_3$ catalysts (Figures 6b and 6c for $7.5Ni\text{-}2.5Co/Al_2O_3$ and $5Ni\text{-}5Co/Al_2O_3$ catalysts, respectively) with a decrease in H_2 and CO_2 yields as time on stream was increased, which is evidence of the lower extension of reforming and water-gas shift reactions when the catalyst was deactivated. The H_2 yield on the Ni/Al_2O_3 catalyst showed an initial stable period for the first 40 min on stream (93.8 %), and then decreased to 62.6% after 103 min on stream. In the case of bimetallic catalysts, a decrease in H_2 yield is observed from the beginning of the reaction, from 92.3 to 50.9 % for 102 min on stream and from 91.0 to 49.3 % for 87 min on stream for $7.5Ni\text{-}2.5Co/Al_2O_3$ and $5Ni\text{-}5Co/Al_2O_3$ catalysts, respectively. Thus, the poor metal dispersion attained in both bimetallic catalysts led to a faster decrease in H_2 yield as reaction proceeded. Conversely, the Co/Al_2O_3 catalyst showed a low H_2 yield at zero time on stream (20.7 %), it then increased to 55 % at 21 min on stream, and finally dropped sharply to 18.0 % after 37 min on stream. The rise in H_2 yield with time on stream revealed the promotion of water gas shift and reforming reactions, which is due, as explained before, to the reduction of partially oxidized cobalt species in the catalyst leading to a higher amount of metal active sites available for these reactions.

It should be noted that these H_2 yields at zero time on stream for the different catalysts correspond to H_2 productions ranging from 9.8 to 10.2 wt. % by mass unit of biomass fed into the pyrolysis step (Eq. (8)). Accordingly, H_2 production on these catalysts decreases as follows: Ni/Al_2O_3 (10.17 wt. %) > $7.5Ni\text{-}2.5Co/Al_2O_3$ (9.94 wt. %) > $5Ni\text{-}5Co/Al_2O_3$ (9.82 wt. %) >> Co/Al_2O_3 (2.3 wt. %). These results (with the exception of the one for Co/Al_2O_3 catalyst) are of the same order as those obtained in previous studies under similar reaction conditions, wherein a commercial catalyst (G90LDP) [95] and several Ni based catalysts prepared using different supports [48], promoters [49,50]

and calcination temperatures [79] were evaluated. Therefore, these results are evidence of the overall efficiency of the two-step pyrolysis reforming process. Other authors reported similar H_2 productions for cobalt active phase when they used it in monometallic and bimetallic catalysts. Thus, Li et al. [44] studied different Co based catalysts supported on Al_2O_3, ZrO_2, SiO_2, MgO, TiO_2 and $BaAl_{12}O_{19}$ (BA) in the steam reforming of the tar from the pyrolysis of wood biomass. The highest catalytic activity was obtained when Co/BA was used, which they attributed to the high dispersion attained on this strongly basic support. Moreover, the highest H_2 production was obtained on Co/BA catalyst (8.5 wt. %), followed by Co/Al_2O_3 catalyst (8.0 wt. %). Similarly, Zhang et al. [96] investigated the catalytic reforming of the volatile stream from biomass pyrolysis on Ni-Co/γ-Al_2O_3, Ni/γ-Al_2O_3, and Co/γ-Al_2O_3 catalysts, obtaining the highest H_2 production on the Ni-Co/γ-Al_2O_3 catalyst (12.1 wt. %) at a reforming temperature of 825 ºC. Regarding Ni supported on Al_2O_3 support, several authors have reported H_2 productions within the mentioned range of values when they carried out biomass pyrolysis and in-line steam reforming. Thus, Xiao et al. [97] carried out a parametric study in a two-stage fluidized bed/fixed bed, and they obtained the highest H_2 production (7.2 wt. % on a dry and ash free basis) when they used wood chips as biomass raw material and Ni/Al_2O_3 as reforming catalyst. Similarly, Cao et al. [98] analyzed the pyrolysis of sewage sludge and in-line steam reforming, wherein they obtained a maximum H_2 production of 11.6 wt. % (on an ash free basis).

The results displayed in Figure 6 for all the catalysts tested are evidence of the increase in catalyst deactivation rate with time on stream, which involves an autocatalytic effect indicating that the main coke precursors are the non-converted oxygenates, since their concentration in the reaction medium was high, and therefore led to fast catalyst deactivation.

Concerning CO yield, it remained almost constant for all the catalysts tested (slightly higher in the case of Ni/Al_2O_3 and both Ni-Co bimetallic catalysts), as it is a consequence of a balance between the attenuation of reforming (Eqs. (10) and (13)) and WGS reactions (Eq.(11)), and its formation by cracking reactions (Eq. (12)). Furthermore, when a higher amount of Co was loaded in the synthesis, CO yield increased, even at zero time on stream, whereas H_2 and CO_2 yields decreased, which reveals the lower performance of cobalt as metal active site in the WGS reaction compared to nickel. Furthermore, the addition of Co to Ni/Al_2O_3 catalyst contributes to this decrease due to the lower active phase dispersion (Table 3).

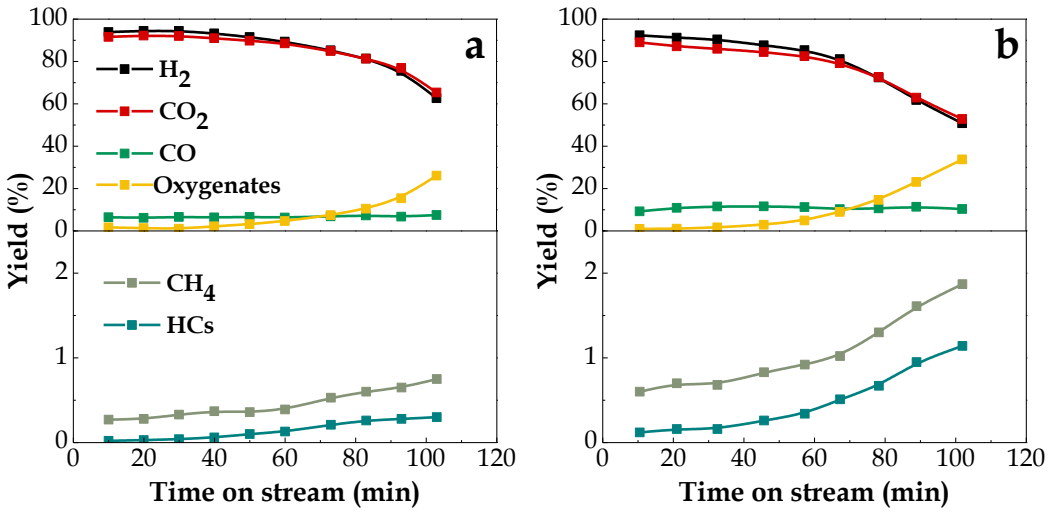

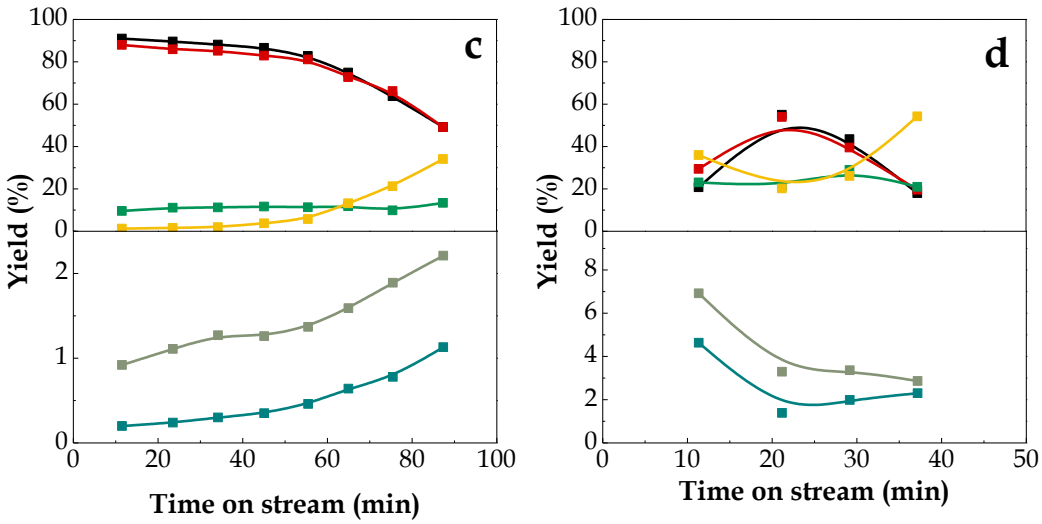

Figure 6. Evolution of the individual product yields with time on stream in the reforming step. a) 10Ni/Al_2O_3, b) 7.5Ni-2.5Co/Al_2O_3, c) 5Ni-5Co/Al_2O_3, and d) 10Co/Al_2O_3 catalysts.

Furthermore, CH_4 and light hydrocarbon yields increased with time on stream when Ni/Al_2O_3 and the two Ni-Co/Al_2O_3 catalysts were used, with this increase being more pronounced in the case of the bimetallic catalysts. This is explained by cracking reactions occurring in the process, although to a low extent, since their yields were lower than 2 % even when the catalysts were deactivated and reforming reactions were attenuated. Nevertheless, CH_4 and light hydrocarbon yields for Co/Al_2O_3 catalyst were significantly higher at zero time on stream (6.9 % and 4.6 %, respectively) due to the reduction of metal active sites by the oxidation of cobalt species with steam prior to the reforming reaction, which hindered reforming and WGS reactions at the expense of promoting cracking ones. As reforming proceeded, reduction of cobalt sites took place and a decrease in CH_4 and HCs yields was observed. However, the concentration of non-converted oxygenated compounds in the reaction medium was noticeable, and therefore fast catalyst deactivation rate was observed after 40 min on stream, which is evidence of the role played by these oxygenated compounds as main coke precursors.

3.3. Deterioration of catalysts properties

The viability of a large-scale catalytic process depends on the design of suitable catalysts, with the greatest challenge being the prevention and attenuation of catalyst degradation. Accordingly, the understanding of the different mechanisms of catalyst activity decay is essential in order to achieve this target. Thus, catalyst deactivation can be a consequence of mechanical, chemical and/or thermal degradation [99]. A detailed characterization of the deactivated catalysts was carried out in order to both ascertain the origin of the deactivation and delve into the understanding of the relationship between the catalysts features and their performance. Thus, the deterioration of catalysts properties is approached in this section. It should be pointed out that a detailed analysis aimed at ascertaining whether sulfur poisoning is a possible cause of catalyst deactivation has not been conducted, and therefore catalyst deactivation by sulfur compounds cannot be discarded. As observed in Table 1, several impurities and organic sulphur compounds may be in the feed, particularly in the biomass ashes. These compounds remained in the char produced in the first pyrolysis step, which was continuously removed. Thus, this two-step reactor configuration has the advantage of avoiding the direct contact of the reforming catalyst with the biomass and its impurities, since they were retained in the pyrolysis reactor. However, a very low concentration of sulfur compounds in the gaseous stream (5-25 ppm) could affect the catalyst performance during steam reforming reaction [100], and therefore a more detailed analysis of the spent catalyst should be carried out in order to exclude sulfur poisoning as a deactivation mechanism.

3.3.1. Mechanical properties

In order to evaluate the possible catalyst attrition during the process, the deactivated samples were sieved in the range of the fresh catalyst particle size. The results obtained

revealed that all deactivated catalysts remained in the range of 0.4-0.8 mm, which evidenced that no particle attrition ocurred during the experimental runs. The results obtained by catalysts sieving confirmed a negligible amount of fines in the filter. Besides, the absence of particle attrition was verified based on the TPO analyses as follows: i) sieving of burnt catalyst particles revealed that particle size did not change (0.4-0.8 mm), and, ii) the difference in the bed mass before and after the pyrolysis-reforming tests corresponds to the amount of coke determined by TPO analyses.

As aforementioned, prior to the catalyst synthesis, the Al_2O_3 support was calcined at 1000 ºC and subsequently fluidized for several hours in order to round the particles, thereby improving their mechanical strength and minimizing possible attrition problems during the reforming step. Besides, the short duration of the experimental runs hindered the possibility of large particle attrition.

3.3.2. Textural properties

The physical properties of the deactivated catalysts are set out in Table 4. In addition, in order to ease the comparison between the fresh and deactivated catalysts, the textural properties of the fresh ones are also displayed in Table 4. As observed, the BET surface area remained almost constant in all deactivated catalysts, which suggests that although catalysts pores may be partially blocked by coke deposition, they were all accessible, i.e., this partial blockage did not lead to a complete clogging of the catalyst pores.

Moreover, pore volume and pore diameter decreased in all the deactivated catalysts, revealing blockage or partial obstruction of biggest pores by the coke deposited on their walls. This reduction in pore volume and pore diameter was more pronounced in the case of Ni/Al_2O_3 catalyst, i.e., from 0.39 to 0.29 $cm^3\ g^{-1}$ and from 182 to 153 Å, respectively. However, similar results were obtained for all the catalysts, revealing that

the content of the metal active phase has no significant influence on the mentioned properties.

Table 4. Textural properties and metal crystallite sizes of the fresh and deactivated catalysts.

Catalysts	S_{BET} (m^2 g^{-1}) fresh/deact.	V_{pore} (cm^3 g^{-1}) fresh/deact.	d_{pore} (Å) fresh/deact.	d_M[a] (nm) fresh/deact.	d_M[b] (nm) deact.
$10Ni/Al_2O_3$	76/75	0.39/0.29	182/153	10/13	13
$7.5Ni\text{-}2.5Co/Al_2O_3$	79/79	0.33/0.29	164/150	24/24	23
$5Ni\text{-}5Co/Al_2O_3$	78/76	0.33/0.28	170/148	24/24	24
$10Co/Al_2O_3$	75/75	0.33/0.29	177/149	13/n.d.	21

[a] Calculated from the full width at half height of the diffraction peak of Ni^0 (2 0 0) and Co^0 (2 0 0) at $2\theta = 52°$ in the XRD, using the Scherrer equation.

[b] Metal crystallite size (d_M, nm) determined from TEM images.

3.3.3. Metallic properties

The changes in the metallic structure after the pyrolysis-reforming reaction may be assessed by comparing the X-ray diffraction (XRD) patterns of the deactivated catalysts shown in Figure 7 with those corresponding to the fresh and reduced catalysts shown above in Figures 3 and 4, respectively.

In the case of Ni/Al_2O_3 catalyst, the diffraction lines at $2\theta = 44º$, 52º and 76º are attributed to crystalline phases of Ni^0 corresponding to planes (1 1 1), (2 0 0) and (2 2 0), respectively [86]. Regarding bimetallic $Ni\text{-}Co/Al_2O_3$ catalysts, these diffraction lines are indistinctly ascribed to Ni^0 and Co^0, since, as mentioned before, both species have similar diffraction angles, and so their separate identification is not possible. It is to note that no significant differences are observed when the reduced and deactivated XRD profiles of Ni/Al_2O_3 and $Ni\text{-}Co/Al_2O_3$ catalysts are compared. Besides, no reflections

ascribed to NiO, Co_3O_4 or CoO are observed, which reveals that their deactivation is not related to the active phase oxidation.

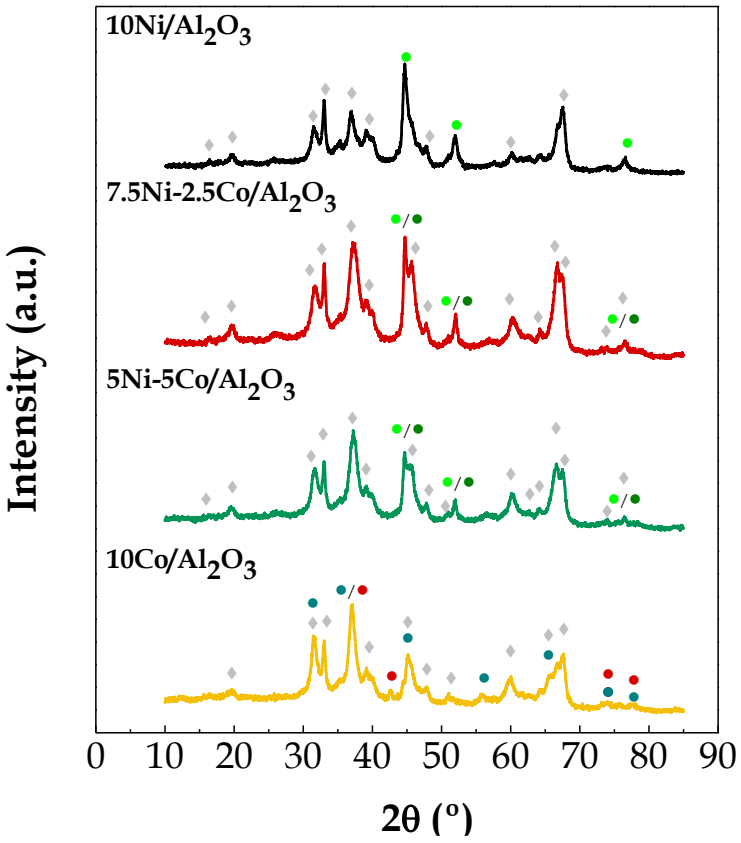

Figure 7. XRD patterns of the deactivated catalysts. Crystalline phases: (♦) Al_2O_3, (●) Ni^0, (●) Co^0 (●) Co_3O_4, and (●) CoO.

However, a comparison of the reduced and deactivated XRD patterns for Co/Al_2O_3 catalyst reveals significant changes in their crystalline structure. As observed, a new diffraction line corresponding to CoO (1 1 1) phase at 2θ = 42° is observed [91], indicating the oxidation of Co^0 active phase under reaction conditions. Moreover, reflections ascribed to Co_3O_4 phases appear at 2θ = 19º, 31º, 37º, 45º, 55º, 59º, and 65º, whereas no diffraction peaks attributed to metallic Co^0 phase are observed. The coincidence of Co_3O_4 and $CoAl_2O_4$ reflection peaks hinders their separate identification. Moreover, the re-oxidation of cobalt metal crystallites on Co/Al_2O_3 catalyst, which is

evident in the XRD spectrum, explains the fast decrease in oxygenate conversion (Figure 5). Besides, as shown before in Figure 4, the steam required in the reforming step caused the oxidation of metallic Co^0 sites, leading to their decrease, and therefore causing the deactivation of this catalyst. Moreover, several authors have analyzed the chemical state of cobalt in Co-based catalysts during the steam reforming reactions by means of several in-situ and operando techniques. Thus, although the oxidation state of Co depends on several factors, such as catalyst structure, particle size, support material and composition of the gas phase in the reaction environment [101], conversion of metallic Co^0 to CoO under steam reforming conditions has been reported. Thus, this occurs by oxidation of Co^0 with the oxygen derived from the dissociative adsorption of the water in the reaction mixture [92,102].

Moreover, oxidation of Co^0 crystallites had not occurred in bimetallic catalysts, which reveals the positive influence of Ni^0 to hinder the transition of Co^0 to inactive cobalt oxide phases through the formation of Ni-Co alloy.

In order to determine the irreversible deactivation by metal sintering, the crystallite size of the deactivated catalysts was determined by the Scherrer equation applied to the diffraction peak at $2\theta = 52°$. Thus, a comparison of the results obtained for the fresh and deactivated catalysts shows that the Ni crystallite size for Ni/Al_2O_3 increased from 10 to 13 nm, and therefore metal sintering may influence the catalyst performance during the reaction. In the case of both bimetallic catalysts, although Ni^0 and Co^0 crystallite sizes cannot be distinguished in the XRD profiles due to the coincidence of their diffraction peaks, the results reveal that no metal sintering had occurred in these catalysts because similar crystallite sizes were obtained (see Table 4). Besides, based on the XRD results, the determination of the crystallite size in Co/Al_2O_3 catalysts was not possible due to the absence of metallic Co^0, which reveals that this catalyst had not undergone

deactivation by metal sintering, but only by the loss of catalytic active phase by oxidation.

3.4. Coke deposition

Once particle failure, sintering and oxidation of the active phase had been analyzed as possible causes of catalyst activity decay, the coke deposited on the deactivated catalysts was characterized by means of different analytical techniques to determine its content, nature and location.

3.4.1. Temperature programmed oxidation (TPO)

The amount of coke deposited on each deactivated catalyst was analyzed by temperature programmed oxidation (TPO), Table 5, and the profiles are displayed in Figure 8. The extent of coke deposition was expressed as wt. % and, given the differences in the stability of the catalysts, the average coke deposition rate per biomass mass unit fed was assessed by considering the different times on stream of the catalysts (see Figures 5 and 6) based on Eq. (3). As observed in Table 5, the active phase selected significantly influenced the total amount of coke deposited during pyrolysis-reforming reactions. Thus, the Ni/Al_2O_3 catalyst had the lowest coke content (2.84 wt. %) and this catalyst is the one in which the average coke deposition rate was lowest (0.37 $mg_{coke}\ g_{cat}^{-1}\ g_{biomass}^{-1}$). This is consistent with the lower deactivation rate observed in Figures 5 and 6 when the evolution of conversion and product yields with time on stream was monitored. In the case of bimetallic Ni-Co based catalysts, the amount of coke deposited on these catalysts was considerable higher (9.41 and 9.24 wt. % for 7.5 Ni-2.5Co/Al_2O_3 and 5 Ni-5Co/Al_2O_3, respectively), which suggests that Co^0 active phase is more prone to coke deposition than Ni^0. It should be noted that, as Ni/Co ratio was reduced in the bimetallic catalysts, the average coke deposition rate increased

considerably, which evidences the correlation between the amount of Co loaded and the coke deposited on these catalysts. The higher particle size observed in the bimetallic catalysts compared to Ni/Al_2O_3 catalyst also influences the higher coke formation rate on $Ni\text{-}Co/Al_2O_3$ catalysts.

Besides, Co/Al_2O_3 catalysts had a high amount of coke deposited, with their average coke deposition rates being the highest (8.85 wt. % and 3.18 $mg_{coke}\ g_{cat}^{-1}\ g_{biomass}^{-1}$, respectively). This is explained by the loss of Co^0 active sites by oxidation during the reforming reaction, which leads to a lower capability for converting oxygenate compounds derived from biomass pyrolysis, and therefore to more severe coke formation.

Table 5. Values of coke content on the deactivated catalysts (C_C) and of average coke deposition rate per biomass mass unit fed (r_C).

Catalyst	Cc (wt. %)	Time on stream (min)	Biomass feed (g)	rc ($mg_{coke}\ g_{cat}^{-1}\ g_{biomass}^{-1}$)
$10\ Ni/Al_2O_3$	2.84	103.0	77.0	0.37
$7.5\ Ni\text{-}2.5Co/Al_2O_3$	9.41	101.9	76.4	1.23
$5\ Ni\text{-}5Co/Al_2O_3$	9.24	87.4	65.5	1.41
$10\ Co/Al_2O_3$	8.85	37.2	27.9	3.18

Nevertheless, other authors have reported a positive influence of adding cobalt to nickel catalysts by reducing coke formation during reforming reactions [41]. Thus, Wang et al. [47] evaluated different $Ni–Co/Al_2O_3$ catalysts and observed that the performance of bimetallic catalysts with the optimum composition was much better than the corresponding monometallic Ni and Co catalysts in terms of catalytic activity, resistance to coke formation and catalyst life in the steam reforming of biomass tar.

Figure 8 shows the TPO profiles of the deactivated catalysts. Based on the temperatures of the combustion peaks in these profiles, several authors have classified the coke

deposited according to two main features: nature and location. Accordingly, depending on the combustion temperature, three main regions can be distinguished [22,103,104]: i) low temperatures corresponding to amorphous coke (hydrogenated composition) or that deposited on metal particles), ii) moderate temperatures corresponding to a more oxygenated coke or that deposited on the metal-promoter and/or metal-support interface, and iii) high temperatures corresponding to a more accessible coke within the catalyst porous structure or that deposited on the support.

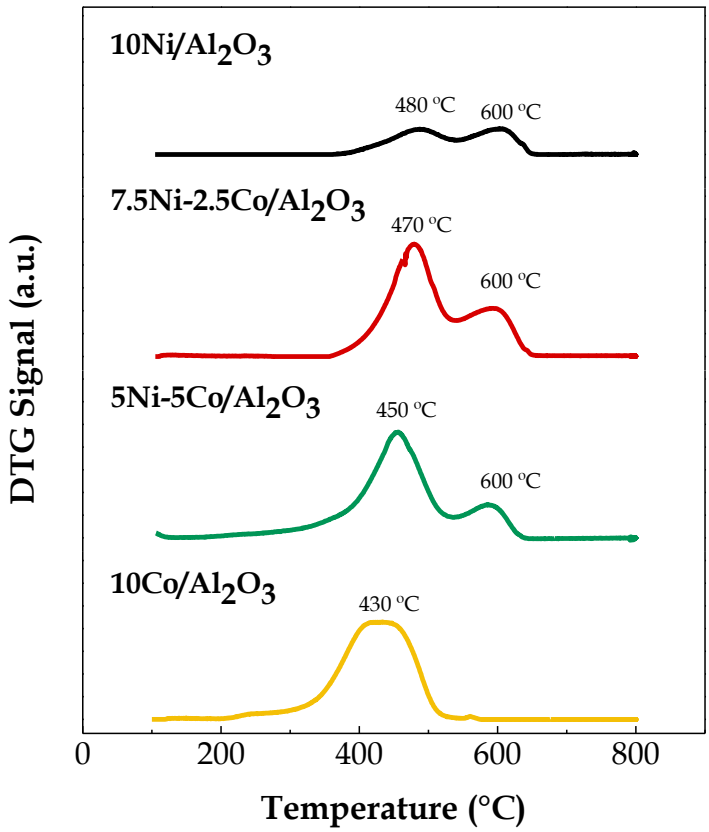

Figure 8. TPO profiles of the deactivated catalysts.

As observed in Figure 8, two main peaks are distinguished in the Ni/Al_2O_3 profile, with the first combustion peak appearing at 480 °C, ascribed to amorphous coke, and the second one at 600 °C, related to a more structured coke. In the case of $Ni\text{-}Co/Al_2O_3$ catalysts, both peaks are observed, with the one located at lower temperature being

more pronounced, which is evidence that the incorporation of Co active phase hindered the evolution of the coke towards a more condensed material. Moreover, as the amount of Co was increased in the catalysts, a slight reduction was observed in the first peak corresponding to the low combustion temperature.

In the case of Co/Al_2O_3 catalyst, one main peak located at low temperature was observed (430 ºC), which is ascribed to amorphous coke. This coke fraction covered the remaining metal particles, which had not been oxidized by the steam in the reaction medium, hindering the access of reactants to the active sites, and is therefore the main responsible for catalyst deactivation [49]. Accordingly, the deactivation of the Co/Al_2O_3 catalyst is not a consequence of a single mechanism, but the combination of multiple factors (metal oxidation and coke deposition), which led to catalyst degradation. Thus, both metal oxidation and coke deposition have a synergistic effect on the catalyst deactivation.

3.4.2. Scanning electron microscopy (SEM)

Figure 9 shows the SEM images of all the deactivated catalysts. These images did not reveal any specific morphology of the coke formed, with no filamentous carbon being observed in any of the deactivated samples. Thus, although the coke evolved to more condensed structures, it was mainly amorphous, as previously discussed in the TPO profiles.

Moreover, the coke deposited on Ni/Al_2O_3 (Figure 9a) was non-uniformly distributed (zones of preferable deposition), whereas a more homogeneous coke was deposited on the surface of both bimetallic Ni-Co catalysts (Figures 9b and 9c corresponding to $7.5Ni\text{-}2.5Co/Al_2O_3$ and $5Ni\text{-}5Co/Al_2O_3$, respectively), with a thin layer covering the catalyst surface. It is to note that Ni^0 and Co^0 species (white spots) cannot be

distinguished from each other due to their similar atomic number, and they appeared in these images slightly faded because of the thin layer of the coke deposited on the catalysts. However, the presence of metallic active sites is clearly evident in the images corresponding to Ni/Al_2O_3 and bimetallic catalysts.

Nevertheless, a lower amount of Co^0 particles is observed on Co/Al_2O_3 catalyst (Figure 9d), whereas cobalt oxide phases are evident (dark spots). Besides, a higher amount of amorphous coke covering cobalt particles is observed.

Other literature results deal with the formation of filamentous coke in reforming reactions, especially in the reforming of bio-oil model compounds, such as ethanol [105] and glycerol [71] and, especially, in the reforming of hydrocarbons [65,106]. However, previous studies of biomass pyrolysis and in-line reforming confirm the lack of this filamentous coke in the mentioned process [95], which is presumably related to the high steam/oxygenate ratio used. Besides, Nabgan et al. [107] evaluated the performance of Ni/La_2O_3, $Ni–Co/La_2O_3$, and Co/La_2O_3 catalysts in the steam reforming of acetic acid, and they observed by SEM images that the coke on the deactivated catalysts does not have any specific morphology, although their images suggested that the carbon formed was partially crystalline, with small crystallite sizes.

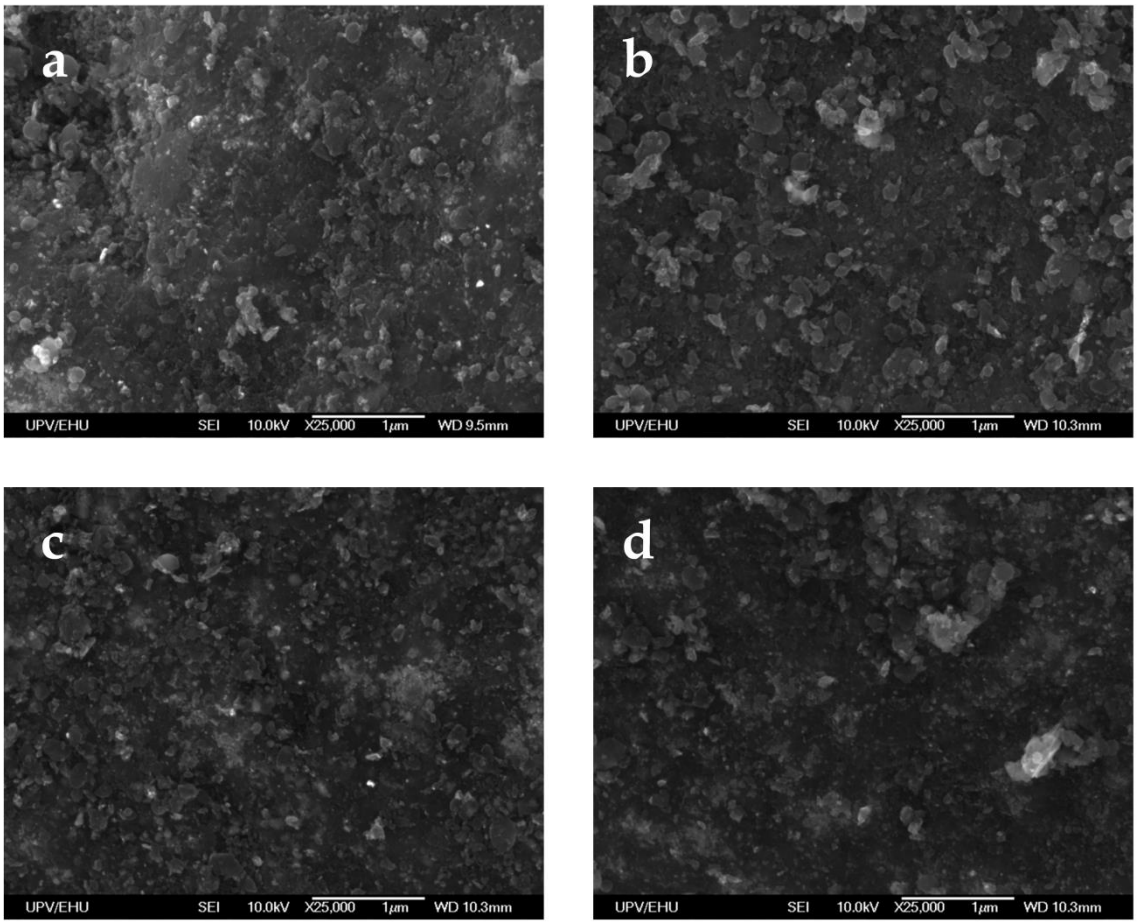

Figure 9. SEM images of deactivated catalysts: a) 10Ni/Al_2O_3, b) 7.5Ni-2.5Co/Al_2O_3, c) 5Ni-5Co/Al_2O_3, and d) 10Co/Al_2O_3 catalysts.

3.4.3. Transmission electron microscopy (TEM)

Figure 10 shows the TEM (transmission electron microscopy) images of all deactivated catalysts. The dark areas correspond to Ni and/or Co particles, whereas the elongated grey shapes are related to the Al_2O_3 support. Besides, the coke deposited on all the catalysts (blurred spots) has no structured morphology, i.e., filamentous coke was not observed, corroborating the amorphous nature previously shown by SEM images.

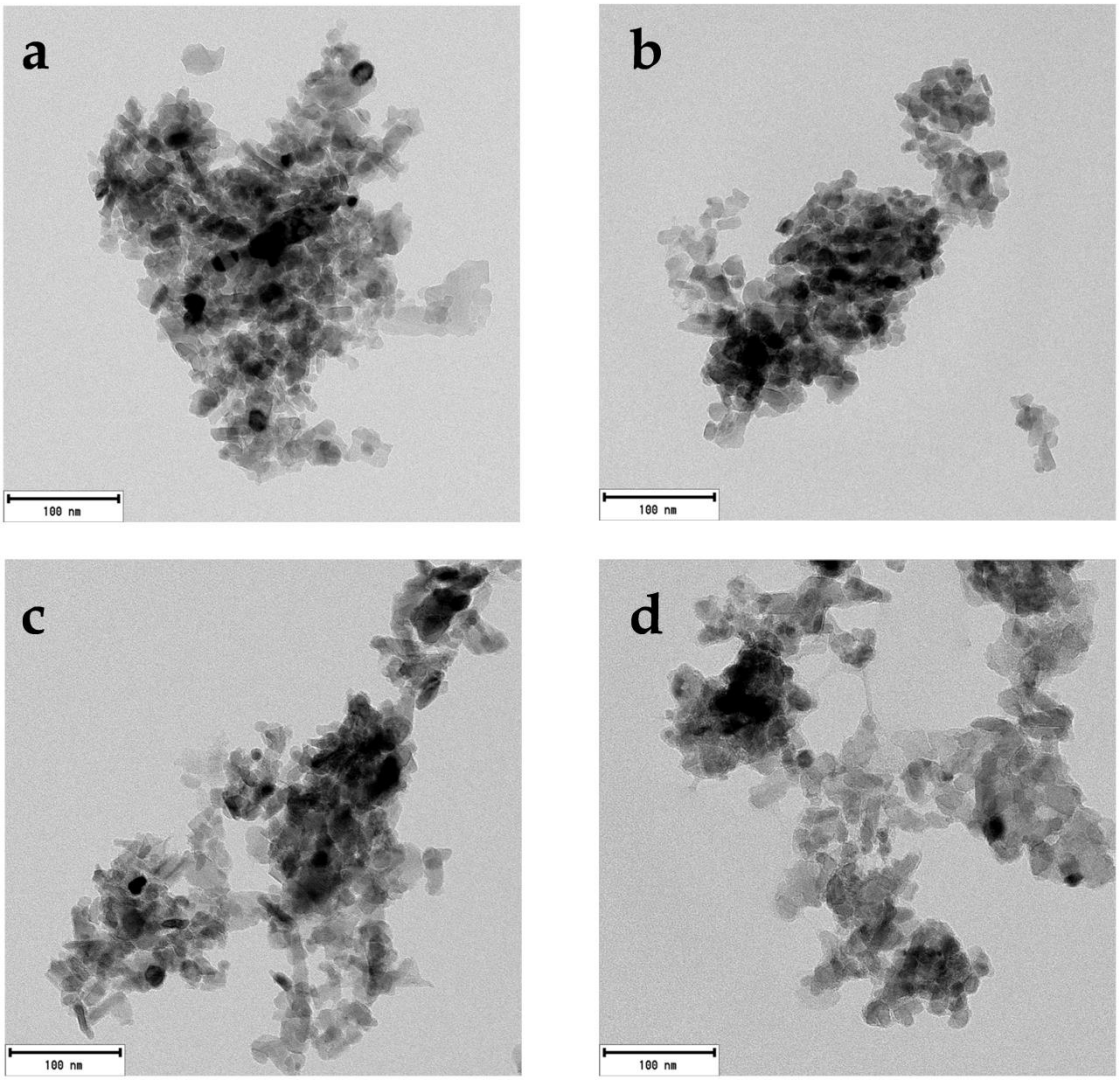

Figure 10. TEM images of deactivated catalysts: a) 10Ni/Al_2O_3, b) 7.5Ni-2.5Co/Al_2O_3, c) 5Ni-5Co/Al_2O_3, and d) 10Co/Al_2O_3 catalysts.

Regarding Ni/Al_2O_3 (Figure 10a) and Ni-Co/Al_2O_3 catalysts (Figures 10b-c), metal particle sizes are in close agreement with those determined by XRD technique.

In the case of Co/Al_2O_3 catalyst (Figure 10d), the following features are worth mentioning: i) lower amount of metal active phase (dark spots) compared to Ni/Al_2O_3 and bimetallic catalysts, ii) bigger particles (slightly darker grey areas), which presumably corresponded to cobalt oxides (CoO and/or Co_3O_4) detected also by XRD (Figure 7), and iii) a high amount of amorphous coke covering both the catalyst surface

and metal particles, which is consistent with the previous results obtained by TPO analysis (Table 5 and Figure 8).

4. Conclusions

The strategy of biomass pyrolysis and in-line steam reforming in a two-step reactor configuration (CSBR-FBR) performs well for H_2 production. In fact, H_2 productions above 10 wt.% are obtained. Moreover, the metal selected as active phase greatly conditions the activity and stability during the process.

The Ni/Al_2O_3 catalyst is the one of best performance, with oxygenate conversion being 73.9 % and H_2 yield 62.6% after 103 min on stream. However, the interaction of Ni with Co forming a Ni-Co alloy plays a key role in the performance of bimetallic catalysts, since the oxidation of Co^0 crystallites is avoided, and therefore the formation of inactive cobalt oxide phases does not occur.

The stability of the bimetallic $Ni\text{-}Co/Al_2O_3$ catalysts is lower as Ni/Co loading is decreased, which is evidence of a better performance of Ni^0 active phase for promoting WGS and reforming reactions. Thus, the lower oxygenate conversion observed on these bimetallic catalysts for the first 50 minutes on stream is related to the poor metal dispersion obtained when Ni and Co are simultaneously used as active phases. Although the bimetallic catalysts have higher TOF than Ni/Al_2O_3 catalysts at 45 min on stream, the large crystallite sizes obtained when Ni and Co are simultaneously used as active phases, and therefore the poor metal dispersion of these bimetallic catalysts, promoted higher coke deposition.

Hence, the fast deactivation observed in these catalysts is due to coke deposition, with the non-converted oxygenate compounds being the main coke precursors, but no metal sintering phenomenon is observed. Thus, the average coke deposition rate per biomass

mass unit fed considerably increases when Co^0 is incorporated into the Ni/Al_2O_3 catalyst, revealing a correlation between the amounts of Co loaded on the catalyst and the coke formation rate.

The poor performance of Co/Al_2O_3 catalyst at zero time on stream is attributed to the oxidizing nature of steam, which favors the conversion of Co^0 into inactive CoO phase. As reaction proceeds, oxygenate conversion increases due to the reducing atmosphere in the reforming reactor, but this catalyst is severely deactivated once 37 min operation has elapsed. The main cause of Co/Al_2O_3 catalyst deactivation is the loss of active phase by oxidation of Co^0 with steam, which leads to the highest average coke deposition rate per biomass mass unit fed (3.18 $mg_{coke}\ g_{cat}^{-1}\ g_{biomass}^{-1}$).

The coke deposited in all deactivated catalysts has an amorphous nature, with no filaments formed in any of the deactivated samples. The TPO profiles reveal that, although the presence of Co^0 in $Ni\text{-}Co/Al_2O_3$ catalysts attenuates the evolution of coke to more graphitic structures, higher average coke deposition rates are attained, which leads to faster catalyst deactivation.

Acknowledgments

This work was carried out with the financial support from Spain's ministries of Economy and Competitiveness (CTQ2016-75535-R (AEI/FEDER, UE) and Science, Innovation and Universities (RTI2018-101678-B-I00 (MCIU/AEI/FEDER, UE)), the European Union's Horizon 2020 research and innovation programme under the Marie Skłodowska-Curie grant agreement No. 823745, and the Basque Government (IT1218-19 and KK-2020/00107).

References

[1] E. Kirtay, Energy Convers. Manage. 52 (2011) 1778-1789. 10.1016/j.enconman.2010.11.010.

[2] B. Pandey, Y.K. Prajapati, P.N. Sheth, Int. J. Hydrogen Energy. 44 (2019) 25384-25415. https://doi.org/10.1016/j.ijhydene.2019.08.031.

[3] A. Arregi, M. Amutio, G. Lopez, J. Bilbao, M. Olazar, Energy Convers. Manage. 165 (2018) 696-719. 10.1016/j.enconman.2018.03.089.

[4] P. Mohanty, K.K. Pant, R. Mittal, Wiley Interdiscip. Rev.: Energy Environ. 4 (2015) 139-155. 10.1002/wene.111.

[5] N. Schmitt, A. Apfelbacher, N. Jäger, R. Daschner, F. Stenzel, A. Hornung, Biofuels, Bioprod. Biorefin. 13 (2019) 822-837. 10.1002/bbb.1980.

[6] P. Zhu, O.Y. Abdelaziz, C.P. Hulteberg, A. Riisager, Curr. Opin. Green Sustainable Chem. 21 (2020) 16-21. https://doi.org/10.1016/j.cogsc.2019.08.005.

[7] S. Pang, Biotechnol. Adv. 37 (2019) 589-597. https://doi.org/10.1016/j.biotechadv.2018.11.004.

[8] J. Ma, S. Shi, X. Jia, F. Xia, H. Ma, J. Gao, J. Xu, J. Energy Chem. 36 (2019) 74-86. https://doi.org/10.1016/j.jechem.2019.04.026.

[9] H. Balat, E. Kirtay, Int. J. Hydrogen Energy. 35 (2010) 7416-7426. 10.1016/j.ijhydene.2010.04.137.

[10] D.B. Levin, R. Chahine, Int. J. Hydrogen Energy. 35 (2010) 4962-4969. 10.1016/j.ijhydene.2009.08.067.

[11] S. Rezania, M.F.M. Din, S.M. Taib, J. Sohaili, S. Chelliapan, H. Kamyab, B.B. Saha, Int. J. Hydrogen Energy. 42 (2017) 20955-20969. 10.1016/j.ijhydene.2017.07.007.

[12] J. Karl, T. Pröll, Renewable Sustainable Energy Rev. 98 (2018) 64-78. 10.1016/j.rser.2018.09.010.

[13] J.A. Melero, J. Iglesias, A. Garcia, Energy Environ. Sci. 5 (2012) 7393-7420. 10.1039/c2ee21231e.

[14] S. Koppatz, C. Pfeifer, H. Hofbauer, Chem. Eng. J. 175 (2011) 468-483. https://doi.org/10.1016/j.cej.2011.09.071.

[15] A. Erkiaga, G. Lopez, M. Amutio, J. Bilbao, M. Olazar, Fuel Process. Technol. 116 (2013) 292-299. 10.1016/j.fuproc.2013.07.008.

[16] A. Remiro, B. Valle, A.T. Aguayo, J. Bilbao, A.G. Gayubo, Energy Fuels. 27 (2013) 7549-7559. 10.1021/ef401835s.

[17] M. Cortazar, J. Alvarez, G. Lopez, M. Amutio, L. Santamaria, J. Bilbao, M. Olazar, Energy Convers. Manage. 171 (2018) 1589-1597. 10.1016/j.enconman.2018.06.071.

[18] R. Parajuli, T. Dalgaard, U. Jørgensen, A.P.S. Adamsen, M.T. Knudsen, M. Birkved, M. Gylling, J.K. Schjørring, Renewable Sustainable Energy Rev. 43 (2015) 244-263. 10.1016/j.rser.2014.11.041.

[19] Y. Chai, N. Gao, M. Wang, C. Wu, Chem. Eng. J. 382 (2020) 122947. https://doi.org/10.1016/j.cej.2019.122947.

[20] X. Xiao, J. Cao, X. Meng, D.D. Le, L. Li, Y. Ogawa, K. Sato, T. Takarada, Fuel. 103 (2013) 135-140. 10.1016/j.fuel.2011.06.077.

[21] A. Arregi, G. Lopez, M. Amutio, I. Barbarias, L. Santamaria, J. Bilbao, M. Olazar, J. Ind. Eng. Chem. 68 (2018) 69-78. https://doi.org/10.1016/j.jiec.2018.07.030.

[22] A. Ochoa, J. Bilbao, A.G. Gayubo, P. Castaño, Renewable and Sustainable Energy Rev. 119 (2020) 109600. https://doi.org/10.1016/j.rser.2019.109600.

[23] C.H. Bartholomew, R.J. Farrauto, Fundamentals of Industrial Catalytic Processes: Second Edition. John Wiley & Sons, Inc., Hoboken, New Jersey, 2010.

[24] M.D. Argyle, C.H. Bartholomew, Catalysts. 5 (2015) 145-269. 10.3390/catal5010145.

[25] D.L. Trimm, Catal. Today. 37 (1997) 233-238. https://doi.org/10.1016/S0920-5861(97)00014-X.

[26] C.H. Bartholomew, Appl. Catal., A. 212 (2001) 17-60. 10.1016/S0926-860X(00)00843-7.

[27] B. Dou, H. Zhang, Y. Song, L. Zhao, B. Jiang, M. He, C. Ruan, H. Chen, Y. Xu, Sustainable Energy Fuels. 3 (2019) 314-342. 10.1039/C8SE00535D.

[28] S. Li, J. Gong, Chem. Soc. Rev. 43 (2014) 7245-7256. 10.1039/C4CS00223G.

[29] G. Guan, M. Kaewpanha, X. Hao, A. Abudula, Renewable Sustainable Energy Rev. 58 (2016) 450-461. 10.1016/j.rser.2015.12.316.

[30] F. Melo, N. Morlanés, Catal. Today. 107-108 (2005) 458-466. https://doi.org/10.1016/j.cattod.2005.07.028.

[31] S.D. Angeli, F.G. Pilitsis, A.A. Lemonidou, Catal. Today. 242 (2015) 119-128. 10.1016/j.cattod.2014.05.043.

[32] G. Vahid Shahed, Z. Taherian, A. Khataee, F. Meshkani, Y. Orooji, J. Ind. Eng. Chem. 86 (2020) 73-80. https://doi.org/10.1016/j.jiec.2020.02.012.

[33] F. Auprêtre, C. Descorme, D. Duprez, Catal. Commun. 3 (2002) 263-267. 10.1016/S1566-7367(02)00118-8.

[34] F. Seyedeyn-Azad, J. Abedi, S. Sampouri, Ind. Eng. Chem. Res. 53 (2014) 17937-17944. 10.1021/ie5034705.

[35] F. Chen, C. Wu, L. Dong, A. Vassallo, P.T. Williams, J. Huang, Appl. Catal., B. 183 (2016) 168-175. 10.1016/j.apcatb.2015.10.028.

[36] N. Gao, C. Quan, Z. Ma, C. Wu, Energy Fuels. 32 (2018) 5234-5243. 10.1021/acs.energyfuels.8b00365.

[37] C. Rioche, S. Kulkarni, F.C. Meunier, J.P. Breen, R. Burch, Appl. Catal., B. 61 (2005) 130-139. 10.1016/j.apcatb.2005.04.015.

[38] R. Xing, V.L. Dagle, M. Flake, L. Kovarik, K.O. Albrecht, C. Deshmane, R.A. Dagle, Catal. Today. 269 (2016) 166-174. 10.1016/j.cattod.2015.11.046.

[39] M.V. Gil, J. Fermoso, C. Pevida, D. Chen, F. Rubiera, Appl. Catal., B. 184 (2016) 64-76. https://doi.org/10.1016/j.apcatb.2015.11.028.

[40] N. Gao, Y. Han, C. Quan, Int. J. Hydrogen Energy. 43 (2018) 22170-22186. https://doi.org/10.1016/j.ijhydene.2018.10.119.

[41] W. Nabgan, T.A. Tuan Abdullah, R. Mat, B. Nabgan, Y. Gambo, S. Triwahyono, Int. J. Hydrogen Energy. 41 (2016) 22922-22931. https://doi.org/10.1016/j.ijhydene.2016.10.055.

[42] F. Bimbela, J. Ábrego, R. Puerta, L. García, J. Arauzo, Appl. Catal., B. 209 (2017) 346-357. https://doi.org/10.1016/j.apcatb.2017.03.009.

[43] K.M. Kim, B.S. Kwak, Y. Im, N. Park, T.J. Lee, S.T. Lee, M. Kang, J. Ind. Eng. Chem. 51 (2017) 140-152. https://doi.org/10.1016/j.jiec.2017.02.025.

[44] D. Li, C. Ishikawa, M. Koike, L. Wang, Y. Nakagawa, K. Tomishige, Int. J. Hydrogen Energy. 38 (2013) 3572-3581. https://doi.org/10.1016/j.ijhydene.2013.01.057.

[45] L. Wang, D. Li, M. Koike, S. Koso, Y. Nakagawa, Y. Xu, K. Tomishige, Appl. Catal., A. 392 (2011) 248-255. 10.1016/j.apcata.2010.11.013.

[46] L. Wang, Y. Hisada, M. Koike, D. Li, H. Watanabe, Y. Nakagawa, K. Tomishige, Appl. Catal., B. 121-122 (2012) 95-104. https://doi.org/10.1016/j.apcatb.2012.03.025.

[47] L. Wang, D. Li, M. Koike, H. Watanabe, Y. Xu, Y. Nakagawa, K. Tomishige, Fuel. 112 (2013) 654-661. https://doi.org/10.1016/j.fuel.2012.01.073.

[48] L. Santamaria, G. Lopez, A. Arregi, M. Amutio, M. Artetxe, J. Bilbao, M. Olazar, Appl. Catal., B. 242 (2019) 109-120. 10.1016/j.apcatb.2018.09.081.

[49] L. Santamaria, M. Artetxe, G. Lopez, M. Cortazar, M. Amutio, J. Bilbao, M. Olazar, Fuel Process. Technol. 198 (2020) 106223. https://doi.org/10.1016/j.fuproc.2019.106223.

[50] L. Santamaria, A. Arregi, G. Lopez, M. Artetxe, M. Amutio, J. Bilbao, M. Olazar, Fuel. 262 (2020) 116593. https://doi.org/10.1016/j.fuel.2019.116593.

[51] A. Arregi, G. Lopez, M. Amutio, I. Barbarias, J. Bilbao, M. Olazar, RSC Adv. 6 (2016) 25975-25985. 10.1039/c6ra01657j.

[52] J. Alvarez, G. Lopez, M. Amutio, J. Bilbao, M. Olazar, Energy Conversion Manage. 181 (2019) 214-222. https://doi.org/10.1016/j.enconman.2018.12.008.

[53] Z. Zhang, X. Hu, J. Li, G. Gao, D. Dong, R. Westerhof, S. Hu, J. Xiang, Y. Wang, Fuel. 217 (2018) 389-403. https://doi.org/10.1016/j.fuel.2017.12.114.

[54] M.A. Aramendía, V. Borau, C. Jiménez, J.M. Marinas, A. Moreno, Colloids Surf. , A. 106 (1996) 161-165. 10.1016/0927-7757(95)03359-9.

[55] L.P.R. Profeti, E.A. Ticianelli, E.M. Assaf, J. Power Sources. 175 (2008) 482-489. 10.1016/j.jpowsour.2007.09.050.

[56] C.R. Ho, V. Defalque, S. Zheng, A.T. Bell, ACS Catal. 9 (2019) 2931-2939. 10.1021/acscatal.8b04612.

[57] D. Li, L. Wang, M. Koike, K. Tomishige, J. Jpn. Pet. Inst. 56 (2013) 253-266. 10.1627/jpi.56.253.

[58] M. Amutio, G. Lopez, M. Artetxe, G. Elordi, M. Olazar, J. Bilbao, Resour. Conserv. Recycl. 59 (2012) 23-31. 10.1016/j.resconrec.2011.04.002.

[59] J. Alvarez, B. Hooshdaran, M. Cortazar, M. Amutio, G. Lopez, F.B. Freire, M. Haghshenasfard, S.H. Hosseini, M. Olazar, Fuel. 224 (2018) 111-120. https://doi.org/10.1016/j.fuel.2018.03.028.

[60] J. Makibar, A.R. Fernandez-Akarregi, M. Amutio, G. Lopez, M. Olazar, Fuel Process. Technol. 137 (2015) 283-289. 10.1016/j.fuproc.2015.03.011.

[61] G. Lopez, J. Alvarez, M. Amutio, N.M. Mkhize, B. Danon, P. van der Gryp, J.F. Görgens, J. Bilbao, M. Olazar, Energy Convers. Manage. 142 (2017) 523-532. 10.1016/j.enconman.2017.03.051.

[62] G. Lopez, M. Olazar, R. Aguado, G. Elordi, M. Amutio, M. Artetxe, J. Bilbao, Ind. Eng. Chem. Res. 49 (2010) 8990-8997. 10.1021/ie1000604.

[63] M. Artetxe, G. Lopez, M. Amutio, G. Elordi, M. Olazar, J. Bilbao, Ind. Eng. Chem. Res. 49 (2010) 2064-2069. 10.1021/ie900557c.

[64] M. Artetxe, G. Lopez, M. Amutio, I. Barbarias, A. Arregi, R. Aguado, J. Bilbao, M. Olazar, Waste Manag. 45 (2015) 126-133. 10.1016/j.wasman.2015.05.034.

[65] I. Barbarias, G. Lopez, M. Artetxe, A. Arregi, L. Santamaria, J. Bilbao, M. Olazar, J. Anal. Appl. Pyrolysis. 122 (2016) 502-510. https://doi.org/10.1016/j.jaap.2016.10.006.

[66] A. Arregi, M. Amutio, G. Lopez, M. Artetxe, J. Alvarez, J. Bilbao, M. Olazar, Energy Convers. Manage. 136 (2017) 192-201. 10.1016/j.enconman.2017.01.008.

[67] I. Barbarias, G. Lopez, J. Alvarez, M. Artetxe, A. Arregi, J. Bilbao, M. Olazar, Chem. Eng. J. 296 (2016) 191-198. 10.1016/j.cej.2016.03.091.

[68] J. Alvarez, G. Lopez, M. Amutio, J. Bilbao, M. Olazar, Bioresour. Technol. 170 (2014) 132-137. 10.1016/j.biortech.2014.07.073.

[69] M.A. Goula, N.D. Charisiou, K.N. Papageridis, A. Delimitis, E. Pachatouridou, E.F. Iliopoulou, Int. J. Hydrogen Energy. 40 (2015) 9183-9200. 10.1016/j.ijhydene.2015.05.129.

[70] X. Zhao, G. Lu, Int. J. Hydrogen Energy. 41 (2016) 3349-3362. 10.1016/j.ijhydene.2015.09.063.

[71] K.N. Papageridis, G. Siakavelas, N.D. Charisiou, D.G. Avraam, L. Tzounis, K. Kousi, M.A. Goula, Fuel Process. Technol. 152 (2016) 156-175. 10.1016/j.fuproc.2016.06.024.

[72] Z. Zhang, X. Hu, L. Zhang, Y. Yang, Q. Li, H. Fan, Q. Liu, T. Wei, C. Li, Fuel Process. Technol. 191 (2019) 138-151. https://doi.org/10.1016/j.fuproc.2019.04.001.

[73] N.D. Charisiou, K.N. Papageridis, G. Siakavelas, L. Tzounis, K. Kousi, M.A. Baker, S.J. Hinder, V. Sebastian, K. Polychronopoulou, M.A. Goula, Top. Catal. 60 (2017) 1226-1250. 10.1007/s11244-017-0796-y.

[74] L. Santamaria, G. Lopez, A. Arregi, M. Amutio, M. Artetxe, J. Bilbao, M. Olazar, Appl. Catal., B. 229 (2018) 105-113. 10.1016/j.apcatb.2018.02.003.

[75] S.S. Itkulova, Y.Y. Nurmakanov, S.K. Kussanova, Y.A. Boleubayev, Catal. Today. 299 (2018) 272-279. https://doi.org/10.1016/j.cattod.2017.07.014.

[76] R.R.C.M. Silva, H.A. Oliveira, A.C.P.F. Guarino, B.B. Toledo, M.B.T. Moura, B.T.M. Oliveira, F.B. Passos, Int. J. Hydrogen Energy. 41 (2016) 6763-6772. https://doi.org/10.1016/j.ijhydene.2016.02.101.

[77] G. Jacobs, Y. Ji, B.H. Davis, D. Cronauer, A.J. Kropf, C.L. Marshall, Appl. Catal., A. 333 (2007) 177-191. 10.1016/j.apcata.2007.07.027.

[78] W. Chu, P.A. Chernavskii, L. Gengembre, G.A. Pankina, P. Fongarland, A.Y. Khodakov, J. Catal. 252 (2007) 215-230. 10.1016/j.jcat.2007.09.018.

[79] L. Santamaria, G. Lopez, A. Arregi, M. Amutio, M. Artetxe, J. Bilbao, M. Olazar, Catal. Sci. Technol. 9 (2019) 3947-3963. 10.1039/c9cy00597h.

[80] G. Jacobs, J.A. Chaney, P.M. Patterson, T.K. Das, B.H. Davis, Appl. Catal., A. 264 (2004) 203-212. https://doi.org/10.1016/j.apcata.2003.12.049.

[81] G. Jacobs, T.K. Das, Y. Zhang, J. Li, G. Racoillet, B.H. Davis, Appl. Catal., A. 233 (2002) 263-281. https://doi.org/10.1016/S0926-860X(02)00195-3.

[82] N. Dewangan, J. Ashok, M. Sethia, S. Das, S. Pati, H. Kus, S. Kawi, ChemCatChem. 11 (2019) 4923-4934. 10.1002/cctc.201900924.

[83] C. Lindfors, P. Mäki-Arvela, P. Paturi, A. Aho, K. Eränen, J. Hemming, M. Peurla, D. Kubicka, I.L. Simakova, D.Y. Murzin, ACS Sustainable Chem. Eng. 7 (2019) 14545-14560. 10.1021/acssuschemeng.9b02108.

[84] V.R. Madduluri, K.S.R. Rao, Catal. Lett. 149 (2019) 3238-3252. 10.1007/s10562-019-02903-7.

[85] L. Chen, C.K.S. Choong, Z. Zhong, L. Huang, Z. Wang, J. Lin, Int. J. Hydrogen Energy. 37 (2012) 16321-16332. 10.1016/j.ijhydene.2012.02.119.

[86] (2003).

[87] J. Zhan, M. Cai, C. Zhang, C. Wang, Electrochimica Acta. 154 (2015) 70-76. https://doi.org/10.1016/j.electacta.2014.12.078.

[88] D. Torres, J.L. Pinilla, I. Suelves, Catalysts. 8 (2018). 10.3390/catal8080300.

[89] B. Valle, B. Aramburu, A. Remiro, J. Bilbao, A.G. Gayubo, Appl. Catal., B. 147 (2014) 402-410. https://doi.org/10.1016/j.apcatb.2013.09.022.

[90] F.G.E. Nogueira, P.G.M. Assaf, H.W.P. Carvalho, E.M. Assaf, Appl. Catal., B. 160-161 (2014) 188-199. https://doi.org/10.1016/j.apcatb.2014.05.024.

[91] E.A. Dorofeeva, A.Y. Postnov, E.A. Pavlova, E.A. Vlasov, M. Peurla, P. Mäki-Arvela, D.Y. Murzin, Catal. Lett. 148 (2018) 512-522. 10.1007/s10562-017-2256-5.

[92] B. Bayram, I.I. Soykal, D. von Deak, J.T. Miller, U.S. Ozkan, J. Catal. 284 (2011) 77-89. https://doi.org/10.1016/j.jcat.2011.09.001.

[93] A. Giehr, L. Maier, S.A. Schunk, O. Deutschmann, ChemCatChem. 10 (2018) 751-757. 10.1002/cctc.201701376.

[94] X.Q. Zhao, S. Veintemillas-Verdaguer, O. Bomati-Miguel, M.P. Morales, H.B. Xu, Phys. Rev. B: Condens. Matter. 71 (2005). 10.1103/PhysRevB.71.024106.

[95] A. Arregi, G. Lopez, M. Amutio, M. Artetxe, I. Barbarias, J. Bilbao, M. Olazar, Fuel. 216 (2018) 233-244. 10.1016/j.fuel.2017.12.002.

[96] Y. Zhang, W. Li, S. Zhang, Q. Xu, Y. Yan, Energy Sources Part A. 35 (2013) 1975-1982. 10.1080/15567036.2011.580327.

[97] X. Xiao, X. Meng, D.D. Le, T. Takarada, Bioresour. Technol. 102 (2011) 1975-1981. 10.1016/j.biortech.2010.09.016.

[98] J.P. Cao, P. Shi, X.Y. Zhao, X.Y. Wei, T. Takarada, Fuel Process. Technol. 123 (2014) 34-40. 10.1016/j.fuproc.2014.01.042.

[99] M.S. Spencer, M.V. Twigg, Annu. Rev. Mater. Res. 35 (2005) 427-464. 10.1146/annurev.matsci.35.100303.120733.

[100] J. Koningen, K. Sjöström, Ind. Eng. Chem. Res. 37 (1998) 341-346. 10.1021/ie970452t.

[101] C. Huck-Iriart, L. Soler, A. Casanovas, C. Marini, J. Prat, J. Llorca, C. Escudero, ACS Catal. 8 (2018) 9625-9636. 10.1021/acscatal.8b02666.

[102] S.S.-. Lin, D.H. Kim, M.H. Engelhard, S.Y. Ha, J. Catal. 273 (2010) 229-235. https://doi.org/10.1016/j.jcat.2010.05.016.

[103] A. Ochoa, A. Arregi, M. Amutio, A.G. Gayubo, M. Olazar, J. Bilbao, P. Castaño, Appl. Catal., B. 233 (2018) 289-300. https://doi.org/10.1016/j.apcatb.2018.04.002.

[104] J.A. Medrano, M. Oliva, J. Ruiz, L. García, J. Arauzo, Energy. 36 (2011) 2215-2224. https://doi.org/10.1016/j.energy.2010.03.059.

[105] I. Rossetti, J. Lasso, E. Finocchio, G. Ramis, V. Nichele, M. Signoretto, A. Di Michele, Appl. Catal., A. 477 (2014) 42-53. 10.1016/j.apcata.2014.03.004.

[106] X. You, X. Wang, Y. Ma, J. Liu, W. Liu, X. Xu, H. Peng, C. Li, W. Zhou, P. Yuan, X. Chen, ChemCatChem. 6 (2014) 3377-3386. 10.1002/cctc.201402695.

[107] W. Nabgan, T.A.T. Abdullah, R. Mat, B. Nabgan, A.A. Jalil, L. Firmansyah, S. Triwahyono, Int. J. Hydrogen Energy. 42 (2017) 8975-8985. 10.1016/j.ijhydene.2016.04.176.